Linear and Nonlinear Electrostatic Oscillations in Nonneutral Electron Plasmas

by

Hiroyuki Higaki

Abstract

In this thesis various aspects of electrostatic oscillations in the nonneutral electron plasma are described, including diocotron oscillations and electron plasma waves.

The theoretical dispersion relation for the linear oscillations of diocotron and electron plasma waves in a cold spheroidal nonneutral plasma is imperfect to describe actual waves in the experimental plasma, because it does not take the boundary condition nor temperature effect into account. It is expected that a spheroidal plasma obeys the Dubin dispersion when the image charge is unimportant. On the other hand, when the plasma becomes longer, the dispersion relation for the cylindrical plasma column is supposed to be applicable. However, there is no experiment for diocotron oscillations of a confined spheroidal nonneutral electron plasma in these intermediate states.

For the reason above, the dispersion relation for the fundamental diocotron oscillation of a spheroidal plasma with a cylindrical boundary was experimentally investigated in these intermediate states. The obtained dispersion relation approaches the one for the cylindrical plasma column as the aspect ratio becomes larger, while it approaches the Dubin dispersion relation as the aspect ratio decreases. This emperically obtained dispersion relation is useful to characterize a spheroidal plasma in this intermediate state, i.e, it is available for the plasma diagnostic without distructive measurement.

So far the temperature dependence of the axisymmetric electrostatic oscillation (the second mode) has been studied up to 0.25 eV for a spheroidal plasma with small electron numbers and the observed frequency shifts have been explained only through computer simulations. A higher density spheroidal nonneutral plasma composed of many particles is becoming more requisite, because they are necessary for production of anti-hydrogen. In such a case, the frequency shift may become larger and a simple method to estimate the shift will be favorable. Therefore, it is important to investigate properties of such a high density plasma.

The frequency shifts in the presence of the cylindrical conducting wall were experimentally observed at room temperature at first. Then, the temperature dependence of the electron plasma oscillations (the second and third mode) were examined for the temperature up to 1.2 eV in plasmas of higher densities with larger total particle numbers. It was shown that the observed frequency shifts can be estimated from the dispersion relation in which the temperature dependence of the dielectric tensor and the frequency shift by the wall effect are included. The dispersion relation modified in this manner makes it easy to estimate the frequency at a given finite temperature. These results revealed the impotance of wall effect when a large spheroidal plasma is confined.

Longitudinal electron plasma oscillations (Langmuir oscillations) in a nonneutral electron plasma column must obey a dispersion relation which is different from that of an unbounded plasma. The present theory states that three wave interaction of Langmuir waves is prohibited in unbounded plasma. But, little attention has been paid to large amplitude Langmuir waves in a confined nonneutral plasma with a finite length.

Through the experiment described here, it was found that a large amplitude Lang-

muir oscillation excited in the confined plasma can transit to the lower modes. When the amplitude of the excited mode is small, the oscillation is governed by Trivelpiece-Gould dispersion relation. However, when the amplitude is large, both sidebands and nonlinear frequency shifts occure. As a result, three wave interaction becomes possible in the non-neutral plasma column. This is the first observation of the three wave nonlinear interaction among Langmuir waves.

Acknowledgements

Contents

Bibliography   75

List of Figures

Chapter 1

Intrduction

A nonneutral plasma is a collection of charged particles, which does not have a charge neutrality as a whole system. One component plasmas (OCP) is a kind of nonneutral plasmas. The words such as nonneutral electron plasma, nonneutral ion plasma, positron plasma and so on are used to describe OCP.

Some works on nonneutral plasmas done before 1970s were mainly concerned with electron beams in microwave generation devices. The main research on nonneutral plasmas arose in 1970s. The theoretical works by R. C. Davidson [1, 2, 3, 4] and the experimental works by J. H. Malmberg [5, 6] facilitated the development of research in this field. Many fundamental investigations, such as equilibrium and stability properties [10, 11], diffusion properties [12, 13, 14], a collisional relaxation of anisotropic temperature [15], a transition to thermal equilibrium [16], plasma waves [5, 6, 17], diocotron instabilities [18, 19], electron cyclotron waves [20, 21, 22, 23], have been performed by many workers. The field has extended to ion plasmas [24, 25], positron plasmas [26, 27, 28, 29, 30, 31, 32, 33] and antiproton plasmas [34]. The nonneutral electron plasma column is also studied as an

excellent example of 2D inviscid fluid [35, 36, 37, 38, 39, 40]. Nonneutral plasmas are studied as strongly coupled plasmas, too. There are several theoretical works on strongly coupled nonneural plasmas [9, 41] and many experimental studies in the laboratories; strongly coupled two dimensional electron plasma on the liquid helium [42], strongly coupled ion plasmas in the Penning trap [43, 44, 45, 46] and strongly coupled dusty plasmas.

The Malmberg trap has been a powerful tool to investigate fundamental properties of the nonneutral plasma column. It is also served as a good container of antimatter, so are the Penning trap and the Paul trap. Although Malmberg trap can confine a large number of particles, its confinement property has problems. The confinement time becomes shorter as the confinement length becomes longer [11]. Furthermore, the confined plasma is not in the ideal rigid rotor equilibrium. These are the fatal defects when we try to confine a large number of (antimatter) particles. The Penning trap [47] and the Paul trap [48] can be used to confine the spheroidal plasma. Their confinements are almost ideal unless the particle number is large. Therefore, it is desirable to improve the confinement apparatus so that it can contain a large number of particles in the rigid rotor equilibrium. The multi-ring electrode trap described in this thesis is one of approaches to develop such an apparatus.

The basic confinement properties of the multi-ring electrode trap were extensively studied by investigating the effect of the electrostatic potential configuration on the confinement time. I could obtain the result that the electrostatic potential $\phi \propto \rho^2 - 2z^2$ gives the better confinement time in the multi-ring electrode trap. This is the same electrostatic potential with that of the Penning trap. However, the multi-ring electrode trap can confine much more particles than the Penning trap, which is comparable to the Malmberg trap. This fact causes another problem. The image charges of the plasma itself or the boundary

cannot be ignored. Thus the potential ϕ mentioned above is not enough for the rigid rotor equilibrium when a lot of particles are confined.

Here, the boundary and temperature effects on the linear dispersion relations of the lowest order diocotron oscillation and lower modes of electron plasma waves are investigated. This kind of experiment has not been done before, since spheroidal plasmas have been confined by Penning trap with less particles (i.e, the wall effect is unimportant). This measurement is important because measured frequencies of these oscillatioins cannot be explained by the theoretical dispersioin relatioin for the cold spheroidal plasma with an infinite boundary. The obtained dispersion relation for the lowest order diocotron oscillation is useful for the diagnosis of the confined plasma. It was found that the measured frequencies of electron plasma waves are explained by considering the frequency shifts caused by the wall and temperature effect.

It is interesting to know not only the properties of linear oscillations but also those of nonlinear oscillations in the multi ring electrode trap. To understand the behaviour of nonlinear oscillations in the nonneutral plasma will give us a good insight into the confinement of the plasmas. Although linear Langmuir waves in the cylindrical plasma are well known as Trivelpiece-Gould mode, little experiment has been done for nonlinear Langmuir waves in a confined cylindrical nonneutral plasma so far. Therefore, the experiment presented in this thesis is important in that this is the first report on the nonlinear Langmuir waves in the confined cylindrical nonneutral plasma. It was found that three wave interaction between Langmuir waves is possible in the cylindrical plasma, which is prohibited against unbounded plasmas.

The results obtained at University of Toronto were also very interesting showing

3

that the ponderomotive force of 1ps laser pulse suppresses the expansion of the high temperature plasma which triggers the onset of the radiative thermal conduction inside the solid SiO_2 target. Threshold intensities for the onset of the radiative thermal conduction were measured for the first time and it was found that it depends on the pulse duration of the laser. I am sure that my stay in Toronto was quite fruitful experience for me in that I could extend my knowledge in physics and learn the international research activity.

The following chapters are constructed as follows. In the next chapter, the theoretical treatment of nonneutral plasmas are briefly reviewed. The multi-ring electrode trap and the basic experimental procedures are described in chapter 3. The linear dispersion relations of diocotron and electron plasma oscillations in the multi-ring electrode trap is discussed in chapter 4 and 5, respectively. The novel features of the nonlinear electron plasma oscillations are treated in chapter 6. The chapter 7 summarizes this thesis. Every result obtained at University of Toronto during my stay as an exchange student is presented in appendix A.

Chapter 2

Theory of nonneutral plasmas

Since there are too many theoretical works on nonneutral plasmas to review, I restrict the contents of this chapter to those which are very fundamental and concerned with experiments described later.

2.1 Equilibrium property

2.1.1 Infinitely long nonneutral plasma column

As a fundamental example, the axially symmetric, infinitely long cold nonneutral electron plasma, which has the radius a and a constant density n inside, is considered in the cylindrical coordinate (r, θ, z). Thus all physical quantity has no azimuthal and axial dependence in the equilibrium. In this case, the plasma density $n(r)$ and the radial electric field $E(r)$ is easily expressed as follows.

$$
n(r) = \begin{cases} n, & 0 \leq r \leq a \\ 0, & a \leq r \end{cases} \quad , \quad E(r) = \begin{cases} -\frac{m}{2e}\omega_p^2 r, & 0 \leq r \leq a \\ -\frac{m}{2e}\omega_p^2 \frac{a^2}{r}, & a \leq r \end{cases} \tag{2.1}
$$
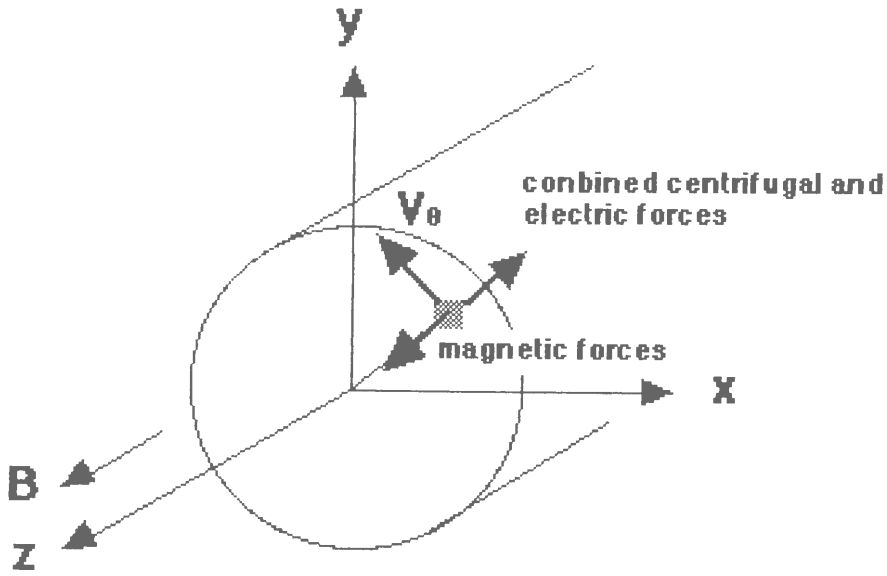
Figure 2.1: *The radial force balance in the infinitely long nonneutral electron plasma column.*

Here, $\omega_p = \sqrt{4\pi n e^2/m}$ is the electron plasma frequency. $-e$ and m are the charge and mass of an electron. Shown in Fig. 2.1, the plasma is radially confined by a uniform axial magnetic field B. The radial force balance equation becomes

$$-\frac{mV_\theta(r)^2}{r} = -eE(r) - \frac{e}{c}V_\theta(r)B \tag{2.2}$$

with $V_\theta(r) = \omega_r(r)r$. Here, c is the speed of light, $V_\theta(r)$ is the equilibrium azimuthal velocity of an electron fluid element and $\omega_r(r)$ is the angular rotation frequency. Substituting eq.(2.1) into eq.(2.2) gives the angular rotation frequency

$$\omega_r(r) = \omega_r^\pm = \frac{1}{2}\Omega_c\left\{1 \pm (1 - \frac{2\omega_p^2}{\Omega_c^2})^{1/2}\right\}. \tag{2.3}$$

6
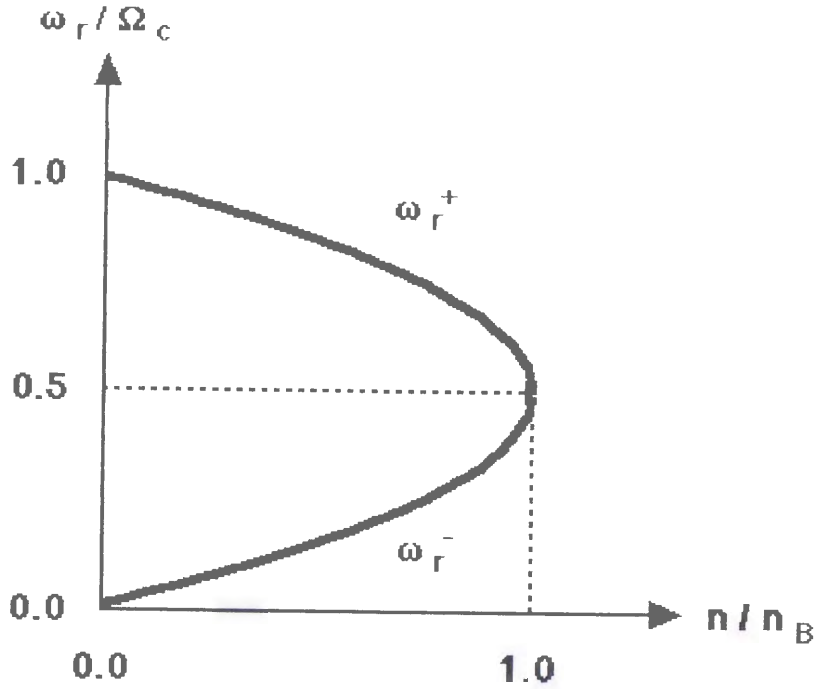
Figure 2.2: *The equilibrium rotation frequency ω_r/Ω_c vs density n/n_B. There are higher and lower rotations for a certain density and there is the Brillouin density limit for a certain B.*

$\Omega_c = eB/mc$ is the electron cyclotron frequency. It can be seen from this expression that $\omega_r(r)$ is independent of radius in the cold nonneutral plasma column, which means that the plasma rotates as a rigid body. Furthermore, there is a maximum density $n_B = B^2/8\pi mc^2$ at a given B, which is called Brillouin density limit. Therefore, the infinitely long nonneutral electron plasma column has a rigid rotor equilibrium with a higher or lower rotation frequency when the plasma density is lower than n_B. The equilibrium rotation frequency is plotted against density in Fig.2.2.

2.1.2 Spheroidal nonneutral plasma

It is seen in the previous subsection that the rigid rotor equilibrium is obtained for the infinitely long cold nonneutral electron plasma with constant density. Although a confined nonneutral plasma in the laboratory has a finite axial length, the rigid rotor equilibrium can be obtained for the special case. That is the cold spheroidal nonneutral plasma which has a constant density n confined with the external electrostatic potential $\phi^{ex}(\rho, z)$ expressed by

$$\phi^{ex}(\rho, z) = -V(\rho^2 - 2z^2)/(2L^2 + b^2). \tag{2.4}$$

This potential $\phi^{ex}(\rho, z)$ is created by the Penning trap which has the axial and radial dimensions L and b, respectively. Let us assume that the spheroidal plasma with axial length $2z_b$ and radius r_b, which is revolving about the z axis, is confined in the Penning trap as shown in Fig.2.3. The self field potential $\phi^s(\rho, z)$ inside the plasma is denoted by

$$\phi^s(\rho, z) = -\frac{m\omega_p^2}{4e}(\gamma r^2 + \beta z^2), \tag{2.5}$$

with

$$\gamma(\alpha) = \frac{1}{1 - (1/\alpha)^2} - \frac{(1/\alpha)^2}{\{1 - (1/\alpha)^2\}^{3/2}} \log\left|\frac{1 + \sqrt{1 - (1/\alpha)^2}}{1 - \sqrt{1 - (1/\alpha)^2}}\right| \tag{2.6}$$

$$\beta(\alpha) = -\frac{2(1/\alpha)^2}{1 - (1/\alpha)^2} + \frac{(1/\alpha)^2}{\{1 - (1/\alpha)^2\}^{3/2}} \log\left|\frac{1 + \sqrt{1 - (1/\alpha)^2}}{1 - \sqrt{1 - (1/\alpha)^2}}\right| \tag{2.7}$$

for $\alpha \equiv z_b/r_b > 1$, i.e., prolate shape. This α is called the aspect ratio of the spheroidal plasma. When $\phi^{ex}(\rho, z) + \phi^s(\rho, z)$ does not depend on z, i.e. depends only on ρ, the spheroidal plasma has the rigid rotor equilibrium. Here, the constant density is the functioin of α and denoted by

$$n(\alpha) = \frac{2V}{\pi e(2L^2 + b^2)\beta(\alpha)}. \tag{2.8}$$

Although the function $\beta(\alpha)$ is modified, the similar expression holds in the case of $\alpha < 1$.
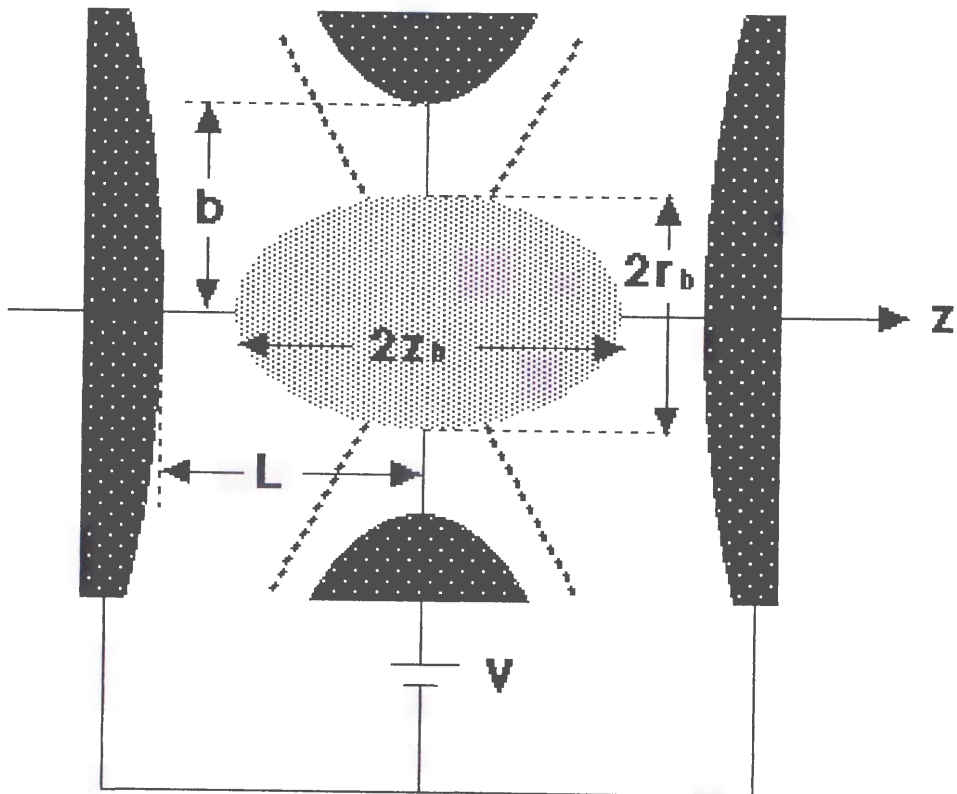
Figure 2.3: *The spheroidal nonneutral plasma in the Penning trap which creates the external potential ϕ^{ex}. The aspect ratio of the plasma is $\alpha \equiv z_b/r_b$.*

2.1.3 Thermal equilibrium

Though the cold plasmas are treated in the previous sections, real plasmas have their finite temperature. The thermal equilibrium of the plasma with uniform temperature T is considered here. The distribution function of the infinitely long nonneutral electron plasma column in the rigid rotor thermal equilibrium is given by

$$f(r,\mathbf{p}) = \frac{n_0}{(2\pi m k_B T)^{3/2}} \exp\left\{-\frac{H - \omega_r P_\theta}{k_B T}\right\} \qquad (2.9)$$

where $H = (p_\rho^2 + p_\theta^2 + p_z^2)/2m - e\phi(\rho)$ is the total energy on individual particle, $P_\theta = \rho(p_\theta - m\rho\Omega_c/2)$ the canonical angular momentum and p_z the axial momentum. And $\phi(\rho)$ is the radial self potential in the equilibrium. Here, k_B is the Boltzmann's constant. An equilibrium density $n(\rho)$ is obtained by integrating the distribution function in the momentum space.

$$n(\rho) = n_0 \exp\left\{-\frac{m}{2k_B T}\left[\rho^2(\omega_r\Omega_c - \omega_r^2) - \frac{2e}{m}\phi(\rho)\right]\right\} \qquad (2.10)$$

It is seen that n_0 is regarded as the density on the axis ($\rho = 0$). It is necessary and sufficient to satisfy $\omega_r\Omega_c - \omega_r^2 - \omega_p^2/2 > 0$ for confining the plasma radially ($n(\rho \to \infty) = 0$). This condition is satisfied in the region surrounded by the curves ω_r^+, ω_r^- and the ordinate in Fig.2.2. The equilibrium density $n(\rho)$ must satisfy the Poisson's equation

$$\frac{1}{\rho}\frac{\partial}{\partial\rho}\rho\frac{\partial}{\partial\rho}\phi(\rho) = n_0 \exp\left\{-\frac{m}{2k_B T}\left[\rho^2(\omega_r\Omega_c - \omega_r^2) - \frac{2e}{m}\phi(\rho)\right]\right\}. \qquad (2.11)$$

This nonlinear Poisson's equation is easily solved as shown in Fig.2.4 [49]. When T is not so high that Debye length $\lambda_D \equiv \sqrt{k_B T/4\pi n e^2}$ is small compared with the plasma size, $n(\rho)$ is almost constant inside the plasma.

The similar discussion can be repeated for the spheroidal nonneutral plasma by replacing $\phi(\rho)$, $n(\rho)$ and $\frac{1}{\rho}\frac{\partial}{\partial\rho}\rho\frac{\partial}{\partial\rho}$ in above equations with $\phi(r,z) = \phi^{ex}(r,z) + \phi^s(r,z)$, $n(\rho,z)$
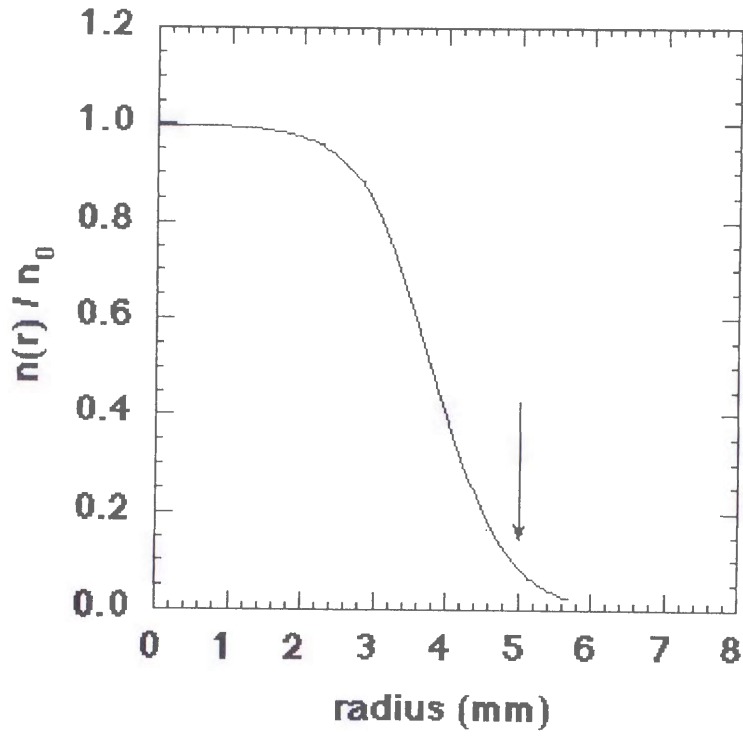
Figure 2.4: *The thermal equilibrium density profile of the infinitely long nonneutral plasma column. When $\lambda_D \ll r_b$, $n(\rho)$ is almost constant inside the plasma.*

and $\frac{1}{\rho}\frac{\partial}{\partial\rho}\rho\frac{\partial}{\partial\rho} + \frac{\partial^2}{\partial z^2}$, respectively. In this system, the total electron number, $N \equiv \int_V n(r,z)dv$, the total canonical angular momentum, $P_\theta^{tot} \equiv \int_V(-\frac{eB}{2c}r^2)n(r,z)dv$ and the electrostatic energy, $E \equiv \int_V(-\frac{e\phi}{2})n(r,z)dv$ are conserved.

2.2   Linear diocotron oscillations

2.2.1   Infinitely long nonneutral plasma column

The purpose of this subsection is to derive the dispersion relation of diocotron oscillations in the infinitely long, cold nonneutral electron plasma column [4]. The continuity equation

$$\frac{\partial}{\partial t}n(\mathbf{x},t) + \frac{\partial}{\partial\mathbf{x}}\cdot n(\mathbf{x},t)\mathbf{V}(\mathbf{x},t) = 0, \tag{2.12}$$

the force balance equation

$$n(\mathbf{x},t)(\frac{\partial}{\partial t} + \mathbf{V}(\mathbf{x},t)\cdot\frac{\partial}{\partial\mathbf{x}})\mathbf{P}(\mathbf{x},t) + \frac{\partial}{\partial\mathbf{x}}\cdot\mathbf{\Phi}(\mathbf{x},t)$$
$$= n(\mathbf{x},t)e(\mathbf{E}(\mathbf{x},t) + \frac{1}{c}\mathbf{V}(\mathbf{x},t)\times\mathbf{B}(\mathbf{x},t)), \tag{2.13}$$

and the Poisson's equation

$$\nabla^2\phi(\mathbf{x},t) = 4\pi en(\mathbf{x},t) \tag{2.14}$$

are the start point. Here, $n(\mathbf{x},t)$ is a density, $\mathbf{V}(\mathbf{x},t)$ a mean velocity, $\mathbf{P}(\mathbf{x},t)$ a mean momentum, $\mathbf{\Phi}(\mathbf{x},t)$ a pressure tensor. Since the cold plasma is considered, the pressure gradient term is neglected. Also, $\phi(\mathbf{x},t)$, $\mathbf{E}(\mathbf{x},t)$ and $\mathbf{B}(\mathbf{x},t)$ denote electric potential, electric and magnetic field, respectively. It is assumed that these quantities are expressed as the sum of equilibrium value and perturbed value as follows.

$$n(\mathbf{x},t) = n(\rho) + \delta n(\mathbf{x},t)$$

$$\mathbf{V}(\mathbf{x},t) = V_\theta(\rho)\hat{\mathbf{e}}_\theta + V_z\hat{\mathbf{e}}_\mathbf{z} + \delta\mathbf{V}(\mathbf{x},t) \tag{2.15}$$

$$\phi(\mathbf{x},t) = \phi(\rho) + \delta\phi(\mathbf{x},t)$$

$$\mathbf{B}(\mathbf{x},t) = B\hat{\mathbf{e}}_\mathbf{z} + \delta\mathbf{B}(\mathbf{x},t)$$

Furthermore, it is assumed that the perturbation depends on time as $\exp(i\omega t)$ and that the θ and z dependence is Fourier decomposed as

$$\delta\psi(\rho,\theta,z,t) = \sum_{l=-\infty}^{\infty}\sum_{k_z=-\infty}^{\infty} \delta\psi^l(\rho,k_z)\exp\{i(l\theta + k_z z - \omega t)\}. \tag{2.16}$$

Thus the eqs. (2.12) $\sim$ (2.14) can be rewritten as

$$-i(\omega - k_z V_z - l\omega_r)\delta n^l + \frac{1}{\rho}\frac{\partial}{\partial\rho}(\rho n \delta V_\rho^l) + il\frac{n\delta V_\theta^l}{\rho} + ik_z n\delta V_z^l = 0, \tag{2.17}$$

$$-i(\omega - k_z V_z - l\omega_r)\delta V_\rho^l - (-\Omega_c + 2\omega_r)\delta V_\theta^l = -\frac{e}{m}\frac{\partial}{\partial\rho}\delta\phi^l, \tag{2.18}$$

$$-i(\omega - k_z V_z - l\omega_r)\delta V_\theta^l + [-\Omega_c + \frac{1}{\rho}\frac{\partial}{\partial\rho}(\rho^2\omega_r)]\delta V_\rho^l = -\frac{e}{m}\frac{il}{\rho}\delta\phi^l, \tag{2.19}$$

$$-i(\omega - k_z V_z - l\omega_r)\delta V_z^l = -\frac{e}{m}ik_z\delta\phi^l, \tag{2.20}$$

$$\frac{1}{\rho}\frac{\partial}{\partial\rho}\rho\frac{\partial}{\partial\rho}\delta\phi^l - \frac{l^2}{\rho^2}\delta\phi^l - k_z^2\delta\phi^l = -4\pi e\delta n^l. \tag{2.21}$$

Substituting eqs. (2.17) $\sim$ (2.20) into the Poisson's equation (2.21) results in the equation

$$\frac{1}{\rho}\frac{\partial}{\partial\rho}\left[\rho\left(1 - \frac{\omega_p^2}{(\omega - k_z V_z - l\omega_r)^2 - (\omega_r^+ - \omega_r^-)^2}\right)\frac{\partial}{\partial\rho}\delta\phi^l\right]$$
$$-\frac{l^2}{\rho^2}\left[1 - \frac{\omega_p^2}{(\omega - k_z V_z - l\omega_r)^2 - (\omega_r^+ - \omega_r^-)^2}\right]\delta\phi^l$$
$$-k_z^2\left[1 - \frac{\omega_p^2}{(\omega - k_z V_z - l\omega_r)^2}\right]\delta\phi^l$$
$$= \frac{l\delta\phi^l}{\rho}\frac{(-\Omega_c + 2\omega_r)}{(\omega - k_z V_z - l\omega_r)}\frac{\omega_p^2}{(\omega - k_z V_z - l\omega_r)^2 - (\omega_r^+ - \omega_r^-)^2}\delta(\rho - \rho_b). \tag{2.22}$$

Here, it is considered that the plasma with uniform density $n(0 \leq \rho \leq \rho_b)$ is surrounded by the cylindrical conducting wall at $\rho = b$ as shown in Fig.2.5. The following relation is

13
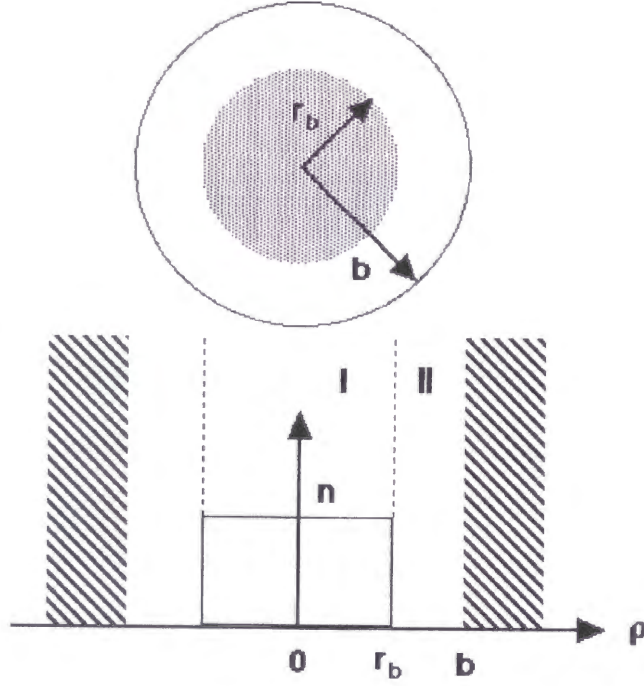
Figure 2.5: *The plasma with uniform density $n(0 \leq \rho \leq \rho_b)$ is surrounded by the conducting wall at $\rho = b$*

used to derive eq.(2.22).

$$\frac{\partial}{\partial \rho} n(\rho) = -n\delta(\rho - \rho_b) \tag{2.23}$$

The eigenvalue equation (2.22) can be solved separately in region I ($0 \leq \rho \leq \rho_b$) and II ($\rho_b \leq \rho \leq b$). In each region eq.(2.22) is represented by

$$\begin{cases} \dfrac{1}{\rho}\dfrac{\partial}{\partial \rho}\rho\dfrac{\partial}{\partial \rho}\delta\phi_I^l - \dfrac{l^2}{\rho^2}\delta\phi_I^l + T^2\delta\phi_I^l = 0, & 0 \leq \rho \leq \rho_b, \\[3mm] \dfrac{1}{\rho}\dfrac{\partial}{\partial \rho}\rho\dfrac{\partial}{\partial \rho}\delta\phi_{II}^l - \dfrac{l^2}{\rho^2}\delta\phi_{II}^l - k_z^2\delta\phi_{II}^l = 0, & \rho_b \leq \rho \leq b. \end{cases} \tag{2.24}$$

with

$$T^2 = -k_z^2\left[1 - \frac{\omega_p^2}{(\omega - k_z V_z - l\omega_r)^2}\right] \Big/ \left[1 - \frac{\omega_p^2}{(\omega - k_z V_z - l\omega_r)^2 - (\omega_r^+ - \omega_r^-)^2}\right] \tag{2.25}$$

14

As the boundary conditions for $\delta\phi^l$, it remains finite at $\rho = 0$, but vanishes on the wall $\rho = b$. At the plasma boundary $\rho = \rho_b$, $\delta\phi^l$ should be continuous. Then the solution is

$$
\begin{cases}
\delta\phi^l_I = AJ_l(T\rho), & 0 \leq \rho \leq \rho_b \\[2mm]
\delta\phi^l_{II} = AJ_l(T\rho_b)\dfrac{[I_l(k_z\rho)K_l(k_zb) - K_l(k_z\rho)I_l(k_zb)]}{[I_l(k_z\rho_b)K_l(k_zb) - K_l(k_z\rho_b)I_l(k_zb)]}, & \rho_b \leq \rho \leq b.
\end{cases}
\tag{2.26}
$$

Here, A is a constant, J_l the Bessel function of the first kind of order l, I_l and K_l are the modified Bessel functions of the first and the second kind of order l. Multiplying the eigenvalue equation (2.22) by ρ and integrating across the surface of the plasma column from $\rho = \rho_b-$ to $\rho = \rho_b+$, we have the equation

$$
\rho_b \left[\frac{\partial}{\partial\rho}\delta\phi^l_{II}\right]_{\rho=\rho_b} - \rho_b \left[1 - \frac{\omega_p^2}{(\omega - k_zV_z - l\omega_r)^2 - (\omega_r^+ - \omega_r^-)^2}\right]\left[\frac{\partial}{\partial\rho}\delta\phi^l_I\right]_{\rho=\rho_b}
$$
$$
= l[\delta\phi^l]_{\rho=\rho_b}\frac{(-\Omega_c + 2\omega_r)}{(\omega - k_zV_z - l\omega_r)}\frac{\omega_p^2}{(\omega - k_zV_z - l\omega_r)^2 - (\omega_r^+ - \omega_r^-)^2}.
\tag{2.27}
$$

Substitution of eq.(2.26) into eq.(2.27) gives the dispersion relation for the electrostatic oscillations in the plasma described in Fig.2.5.

$$
\frac{1}{g_l} - \left[1 - \frac{\omega_p^2}{(\omega - k_zV_z - l\omega_r)^2 - (\omega_r^+ - \omega_r^-)^2}\right]T\rho_b\frac{J_l'(T\rho_b)}{J_l(T\rho_b)}
$$
$$
= l\frac{(-\Omega_c + 2\omega_r)}{(\omega - k_zV_z - l\omega_r)}\frac{\omega_p^2}{(\omega - k_zV_z - l\omega_r)^2 - (\omega_r^+ - \omega_r^-)^2}
\tag{2.28}
$$

with

$$
g_l = \frac{1}{k_z\rho_b}\frac{I_l(k_z\rho_b)K_l(k_zb) - K_l(k_z\rho_b)I_l(k_zb)}{I_l'(k_z\rho_b)K_l(k_zb) - K_l'(k_z\rho_b)I_l(k_zb)}
\tag{2.29}
$$

When diocotron oscillations ($k_z = 0$) are considered, eq.(2.28) can be simplified.

$$
l\frac{(\rho_b/b)^{2l} + 1}{(\rho_b/b)^{2l} - 1} - l\left[1 - \frac{\omega_p^2}{(\omega - l\omega_r)^2 - (\omega_r^+ - \omega_r^-)^2}\right]
$$
$$
= l\frac{\omega_p^2(-\Omega_c + 2\omega_r)}{(\omega - l\omega_r)[(\omega - l\omega_r)^2 - (\omega_r^+ - \omega_r^-)^2]}
\tag{2.30}
$$

15
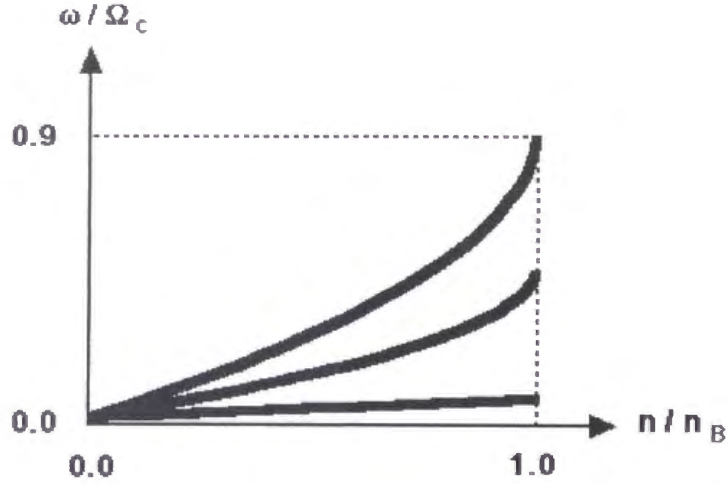
Figure 2.6: $l = 1, 2$ and 3 diocotron frequencies normalized by Ω_c are plotted against density with $\rho_b/b = 0.5$.

This dispersion relation can be easily solved for the eigen frequency ω which is represented by

$$\omega = l\omega_r + \left(\frac{1}{2}\Omega_c - \omega_r\right) \pm \left\{\left(\frac{1}{2}\Omega_c - \omega_r\right)^2 + \frac{1}{2}\omega_p^2\left[1 - (\frac{\rho_b}{b})^{2l}\right]\right\}^{1/2}. \tag{2.31}$$

The high and low frequency solutions correspond to electron cyclotron oscillations and diocotron oscillations of mode l, respectively. The diocotron frequencies ω/Ω_c for $l = 1, 2$ and 3 with $\rho_b/b = 0.5$ are plotted against density n/n_B in Fig.2.6. When the plasma density is low ($\omega_p \ll \Omega_c$), which is satisfied in the experiments described later, a series of diocotron frequencies becomes linear function of the density.

$$\omega = \omega_D[l - 1 + (\frac{\rho_b}{b})^{2l}]. \tag{2.32}$$

Here, $\omega_D \equiv \omega_p^2/2\Omega_c$ is referred to diocotron frequency.

Shown in Fig.2.7 are the schematic drawings of the diocotron oscillations of the nonneutral plasma surrounded by the conducting wall.

16

$l = 1$ $l = 2$

$l = 3$ $l = 4$
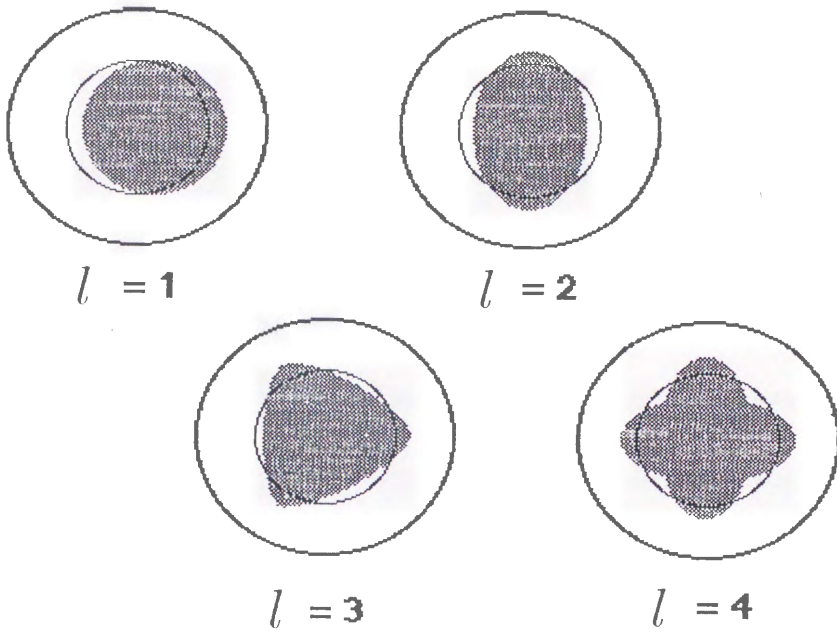
Figure 2.7: *Schematic drawings of lower modes diocotron oscillations of the nonneutral plasma column surrounded by the conducting wall.*

2.2.2 Spheroidal nonneutral plasma

The dispersion relation for electrostatic oscillations in the cold spheroidal nonneutral plasma can be also derived [50, 51]. It is assumed without the loss of generality that the perturbed potential ψ has an azimuthal and time dependence of $\exp i(m\theta - \omega t)$ in the frame rotating with the plasma. Then ψ satisfies the following Poisson's equation.

$$\nabla \cdot \epsilon \cdot \nabla \psi = 0, \quad with \quad \epsilon = \begin{pmatrix} c_1 & -ic_2 & 0 \\ ic_2 & c_1 & 0 \\ 0 & 0 & c_3 \end{pmatrix} \tag{2.33}$$

Here, $c_1 = 1 - \omega_p^2/(\omega^2 - \Omega_v^2)$, $c_2 = \Omega_v\omega_p^2/\omega(\omega^2 - \Omega_v^2)$, $c_3 = 1 - \omega_p^2/\omega^2$ and $\Omega_v = \Omega_c - 2\omega_r$.

Therefore, eq.(2.33) becomes simple Laplace's equation $\nabla^2\psi^o = 0$ outside the plasma whereas inside the plasma it becomes $\{c_1(\partial^2/\partial x^2 + \partial^2/\partial y^2) + c_3\partial^2/\partial z^2\}\psi^i = 0$. These equations seem unseparable since the equations have the cylindrical symmetry and ψ^i has the spheroidal symmetry. However, it is separable in the spheroidal coordinates (ξ_1, ξ_2, ϕ) which are determined by

$$\begin{aligned} x &= [(\xi_1^2 - d^2)(1 - \xi_2^2)]^{1/2}\cos\theta \\ y &= [(\xi_1^2 - d^2)(1 - \xi_2^2)]^{1/2}\sin\theta \\ z &= \xi_1\xi_2 \end{aligned} \tag{2.34}$$

for the outside of the plasma, where $d^2 = z_b^2 - r_b^2$, and the definitions of z_b and r_b are the same as before. To make the operator of eq.(2.33) Laplacian inside the plasma, the spheroidal coordinate $(\xi_1, \bar{\xi}_2, \phi)$ should be used by replacing $z \to z = z(c_1/c_3)^{1/2}$, $\xi_1 \to \xi_1$, $\xi_2 \to \bar{\xi}_2$, and $d^2 \to \bar{d}^2 = z_b^2(c_1/c_3) - r_b^2$. Then the solution ψ, which satisfies the condition that ψ vanishes at infinity and remains finite at the origin is given by

$$\psi^o = AQ_l^m(\xi_1/d)P_l^m(\xi_2)\exp^{i(m\theta-\omega t)}$$

18

$$\psi^i = B P_l^m(\xi_1/d) P_l^m(\xi_2) \exp^{i(m\theta - \omega t)} \tag{2.35}$$

P_l^m and Q_l^m are associated Legendre functions of the first and second kinds. Furthermore, ψ must satisfy $\psi^i = \psi^o|_S$ and $\mathbf{n} \cdot \epsilon \cdot \nabla \psi^i = \mathbf{n} \cdot \nabla \psi^o|_S$ at the plasma boundary, which leads to the equations below

$$B P_l^m = A Q_l^m$$

$$B[(b/d)\epsilon_3 P_l^{m\prime} + m\alpha^2 \epsilon_2 P_l^m] = A(b/d) Q_l^m. \tag{2.36}$$

The presence of the nontrivial solution results in the dispersion relation

$$\epsilon_3 + m\alpha\left(\alpha^2 - \frac{\epsilon_3}{\epsilon_1}\right)^{1/2} \frac{P_l^m(k_1)}{P_l^{m\prime}(k_1)}\epsilon_2 - \frac{k_2}{k_1}\frac{P_l^m(k_1)Q_l^{m\prime}(k_2)}{P_l^{m\prime}(k_1)Q_l^m(k_2)} = 0. \tag{2.37}$$

Here, $k_1 = \alpha(\alpha^2 - \epsilon_3/\epsilon_1)^{-1/2}$ and $k_2 = \alpha(\alpha^2 - 1)^{-1/2}$. The modes of the electrostatic oscillations in the spheroidal nonneutral plasma are expressed with integers (l, m). The mode $(l, 0)$ is an axially symmetric electron plasma oscillation which will be treated in the next section and chapter 5.

The mode (l, l) denotes a diocotron oscillation which corresponds to the mode l diocotron oscillation in the cylindrical plasma column. In fact, eq.(2.37) reduces to

$$\omega = \{-\Omega_v + \sqrt{\Omega_v^2 + 4\omega_p^2[1 - Q_l^{l\prime}/lQ_l^l\alpha(\alpha^2 - 1)^{1/2}]^{-1}}\}/2, \tag{2.38}$$

and eq.(2.35) becomes $\psi^i \propto \rho^l \exp[i(l\theta - \omega t)]$ for the mode (l, l). As ψ^i does not depend on z, it is easily understood that the mode (l, l) corresponds to diocotron oscillations of the spheroidal plasma. Since eq.(2.37) is the dispersion relation in the frame rotating with the plasma, the diocotron frequency in the laboratory frame is $\omega_{lab} = \omega_r - \omega$.

2.3 Linear electron plasma oscillations

2.3.1 Infinitely long nonneutral plasma column

When the nonneutral plasma column without the cylindrical boundary is considered, the continuity equation (2.12), the force balance equation (2.13), eq.(2.9) and Poisson's equation (2.14) lead to the Bohm-Gross dispersion relation $\omega^2 = \omega_p^2(1 + 3k_z^2\lambda_D^2)$. However, this is not suitable to explain the dispersion relation of electron plasma waves in the plasma surrounded by the cylindrical conducting wall. Although temperature is ignored, the Trivelpiece-Gould dispersion is more suitable from this point of view. In this model it is assumed that the plasma column with constant density n fills the cylindrical conducting wall of the radius b. The dispersion relation becomes $J_l(Tb) = 0$, since $g_l \to 0$ in eq.(2.28). Introducing p_{lm} as the m'th zero of J_l and the effective perpendicular wave number $k_\perp \equiv p_{lm}/b$, the dispersion relation can be rewritten as

$$1 - \frac{k_\perp^2}{k^2}\frac{\omega_p^2}{(\omega - k_z V_z - l\omega_r)^2 - (\Omega_c^2 - 2\omega_p^2)} - \frac{k_z^2}{k^2}\frac{\omega_p^2}{(\omega - k_z V_z - l\omega_r)^2} = 0. \tag{2.39}$$

This equation is easily solved for ω with $l = 0$ and $V_z = 0$.

$$\omega^2 = \frac{1}{2}(\Omega_c^2 - \omega_p^2)\left\{1 \pm \left[1 - \frac{k_z^2}{k_z^2 + k_\perp^2}\frac{4\omega_p^2(\Omega_c^2 - 2\omega_p^2)}{\Omega_c^2 - \omega_p^2}\right]^{1/2}\right\} \tag{2.40}$$

This is the Trivelpiece-Gould dispersion relation for the cold plasma column filling the cylindrical boundary. Unfortunately, the exact dispersion relation for electron plasma waves in the nonneutral electron plasma column, which has the gap between the plasma and the boundary, has not been obtained theoretically. There is not the exact dispersion relation for the axially confined plasma column either. The eigenvalue equation

$$\frac{1}{r}\frac{\partial}{\partial r}(r\epsilon_\perp\frac{\partial\phi}{\partial r}) - k^2\epsilon_{\parallel}\phi = 0 \tag{2.41}$$

20
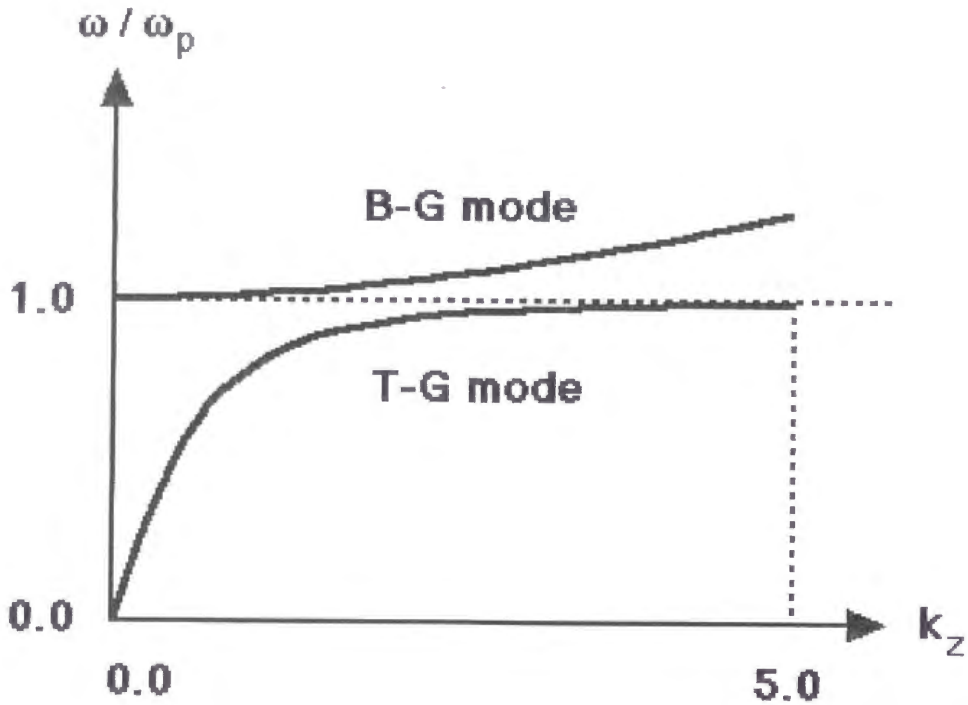
Figure 2.8: *The difference of the dispersion relations for electron plasma waves with and without the boundary.*

for axially symmetric electrostatic waves with boundary condition gives the dispersion relation. It was confirmed that linear dispersion relations observed experimentally agreed with numerical calculations. Taking into account that the axial extent of the plasma is finite, the actual dispersion relation becomes discrete. Bohm-Gross and Trivelpiece-Gould dispersion relations are plotted for the same plasma density in Fig.2.8.

2.3.2 Spheroidal nonneutral plasma

The axially symmetric (m=0 in eq.(2.37)) electron plasma oscillations in a spheroidal nonneutral plasma in the limit of the strong magnetic field $\omega_p \ll \Omega_c$ is represented by the
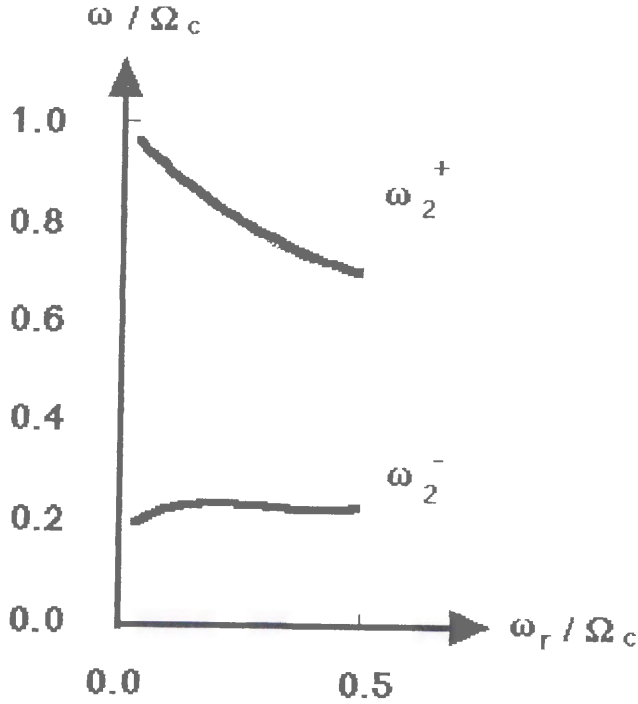
Figure 2.9: ω_2 has two solutions $\omega_2^{\pm}$ in the dispersion relation.

dispersion relation

$$c_3 - \frac{k_2}{k_1}\frac{P_l(k_1)Q_l'(k_2)}{P_l'(k_1)Q_l(k_2)} = 0 \tag{2.42}$$

with $c_1 \to 1$. P_l and Q_l are the first and the second kind of Legendre function of order l. When $l = 1$, it reduces $\omega_1 = \sqrt{4eV/m(2L^2 + b^2)}$ with eq. (2.8). This means that $l = 1$ electron plasma oscillation is regarded as the harmonic oscillation in the ϕ^{ex}. When $l = 2$, eq. (2.42) has two solutions $\omega_2 \pm$. These are plotted against α in Fig.2.9.

2.4   Nonlinear electron plasma oscillations

As mentioned in the abstract, nonlinear electron plasma waves are mainly investigated in the neutral plasma. For examples, parametric coupling between electron-plasma

22

and ion-acoustic oscillations [52], excitation of lower hybrid oscillations at upper hybrid resonance by microwaves [53], nonlinear decay instability and parametric amplification of cyclotron harmonic plasma waves [54], spatial collapse of beam-driven plasma waves [55], sideband instability in a large amplitude electron plasma wave [56], nonlinear frequency shift of an electron plasma wave [57], etc [58, 59, 60]. However, nonlinear electron plasma waves in a nonneutral plasma column also has an interesting feature which will be described in a later chapter. Here, some related theoretical topics are summarized briefly.

The ratio of the energy density W of electrostatic oscillations to the plasma particle energy density nk_BT is used to classify the nonlinear processes in the plasma [61]. It is assumed that $1/n\lambda_D^3 \ll W/nk_BT \ll 1$. Furthermore, the critical energy density W_c is introduced. W_c corresponds to the wave energy density with which the nonlinear frequency broadening is equal to the frequency difference of interacting waves. When $W \ll W_c$, the nonlinear wave-wave interaction results in the decay instability. In this process, interacting waves satisfy $\omega_k = \omega_{k'} \pm \omega_{k''}$ and $k = k' \pm k''$. Here, ω_k is the angular rotation frequency of the wave which has the wave number k. Although there are other nonlinear processes such as the nonlinear Landau damping and the modulational instability, we focus our attention on the decay instability. According to the theoretical treatment for an unbounded neutral plasma, three wave processes $\omega_k \to \omega_{k'} + \omega_{k''}$ leads to the parallelogram on $\omega - k$ plane as shown in Fig.2.10. A remarkable feature in this phenomenon is that it has a certain power threshold for initial pump waves. By using the damping rate $\Gamma_{k'}$ and $\Gamma_{k''}$ of the waves, it is shown that the threshold for this process is proportional to $4\omega_{k'}\omega_{k''}\Gamma_{k'}\Gamma_{k''}$ [62, 63]. The process in which a Langmuir wave decays into two Langmuir waves are forbidden in the
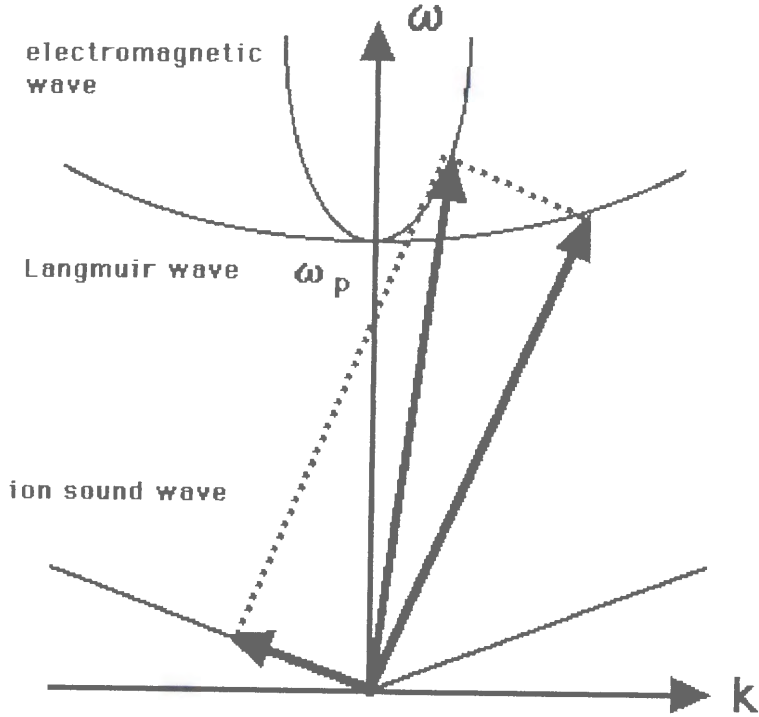
Figure 2.10: *A typical decay instability in which an electromagnetic wave decays into an electron plasma wave and an ion acoustic wave.*

unbounded plasma. Because the energy conservation law

$$\omega_k = \omega_{k'} + \omega_{k''} \tag{2.43}$$

is not satisfied, that is, it is impossible to construct a parallelogram only with the dispersion curve of Langmuir waves. In fact, the dispersion relation of Langmuir waves are dominated by the boundary condition and the density distribution. In the plasma surrounded by the cylindrical boundary, the dispersion of Langmuir waves becomes as shown in Fig.2.8, so that equation (2.43) might be satisfied.

Chapter 3

Multi-ring electrode trap

In this chapter, the experimental apparatus and the experimental procedure are described briefly. As mentioned in the Introduction, the multi-ring electrode trap (MRE trap) can provide the axially long confinement geometry which leads to confinement of a spheroidal nonneutral electron plasma with large α and volume. Also the fact that the MRE trap has many electrodes means that the applied potentioal can be controlled easily.

3.1   Apparatus

To trap nonneutral electron plasmas, the multi-ring electrode trap shown in Fig.3.1 is used. The uniform axial magnetic field B for the radial confinement and the electrostatic potential $\phi^{ex}(r,z)$ for the axial confinement are supplied. Eleven ring electrodes of 3 cm inner radius are aligned along the axis with the same pitch of 1.2 cm, and tungsten mesh electrodes are set on each endside of the trap. These ring electrodes ($No.2 \sim 12$) are connected through resisters and also used as probes. Outer most mesh electrodes ($No.1, 13$) are negatively biased to V to form the electrostatic potential $\phi^{ex}(r,z)$ for the trapping.
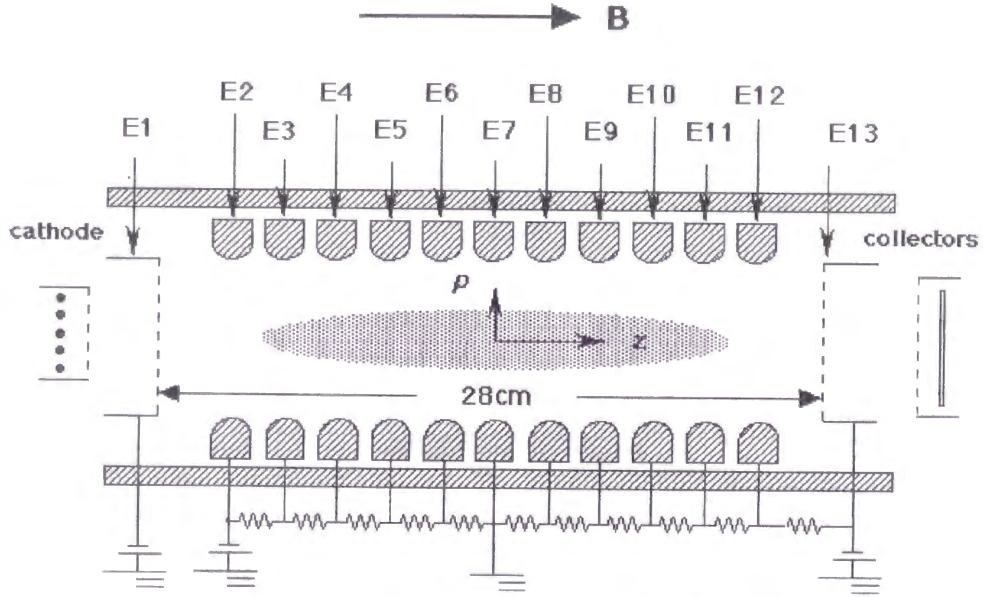
Figure 3.1: *The multi-ring electrode trap composed of 11 ring electrodes and end meshes.*

Each ring electrode numbered by 4, 7 and 10 is azimuthally divided into four sectors for observing axially asymmetric motion of the plasma such as diocotron and cyclotron oscillations. These aligned ring electrodes are regarded as a cylindrical wall against plasma oscillations when axial wave lengths are larger than the pitch of the ring alignment. A cathode of a spiral tungsten wire is set outside the confinement region and also a set of collectors are installed on the other side to measure the total electron number N and the radial profile of axially line-integrated density. At the present experiment described here, $V = -23$ V and $B = 280$ or 700 G. The vacuum chamber is evacuated to 8×10^{-8} Torr. The total axial length available for plasma confinement is 28 cm. The experimental setup as a whole is shown in Fig.3.2
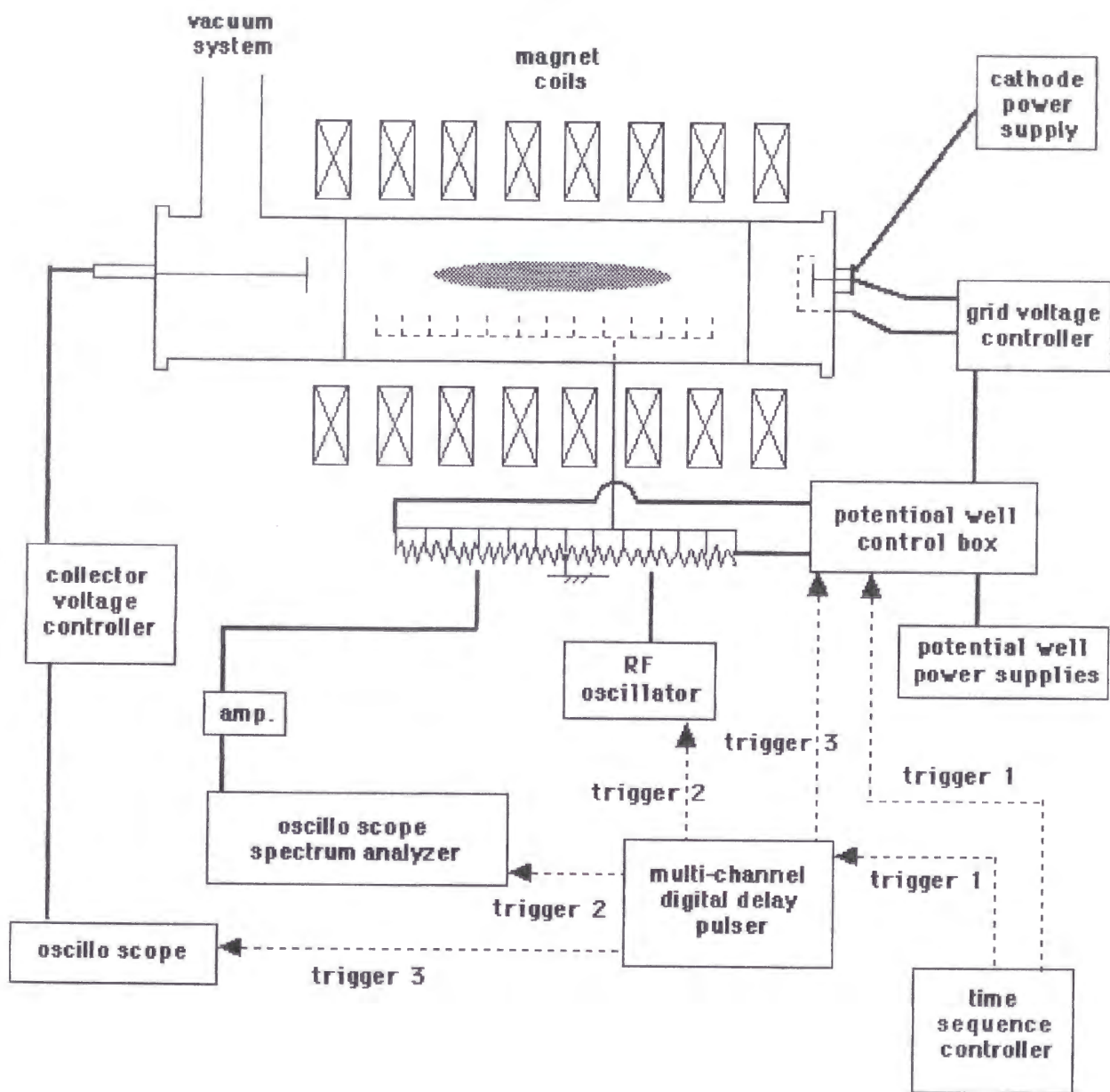
Figure 3.2: *The entire experimetnal system is shown schematically.*

27

3.2 Procedure

The experimental procedure is as follows. At first, the potential applied to $No.1$ mesh electrode is slightly raised from $V = -23$ V so that electrons can flow into the confinement region. After 9ms injection of electrons, the potential of the electrode is returned to $V = -23$ V and electrons are confined in the confinement region. Trapped electrons are cooled through collisions with background neutrals. The plasma temperature becomes less than 0.1 eV within 300ms after injection. The electron cyclotron heating of about 784 MHz or rf heating of ~ 14 MHz is used for controlling the plasma temperature up to 1.5 eV. Then at a constant temperature, the fixed power of RF perturbation is applied to excite the diocotron wave or axially symmetric Langmuir wave with an appropriate electrode. Oscillations of a plasma are detected with other ring electrodes after the excitation signal is ceased. The mode of the excited oscillation is identified with the phase difference of oscillation signals from each ring electrode. Immediately after the oscillation measurement, electrodes $No.13$ are grounded and the trapped electrons flow into the collectors, with which N and the radial profile are measured. This procedure is shown in Fig.3.3. When a plasma temperature is measured, a potential of $No.13$ electrode is damped to V_d. Measurement of leaked electron numbers is repeated at various V_d. A high energy tail of integrated distribution function is obtained by plotting electron numbers against V_d. In this way, the plasma temperature is obtained by assuming a Maxwell distribution. An example of data is shown in Fig.3.4. Also shown in Fig.3.5 is an example of the measured line integrated radial profile. Each point is measured with one of the segmented collectors, which has a diameter of $2r_c=3.4$mm. Since these profiles are line integrated along z axis, they become bell-shaped profiles. In Fig.3.5, the solid circles, open circles and solid triangles correspond

28
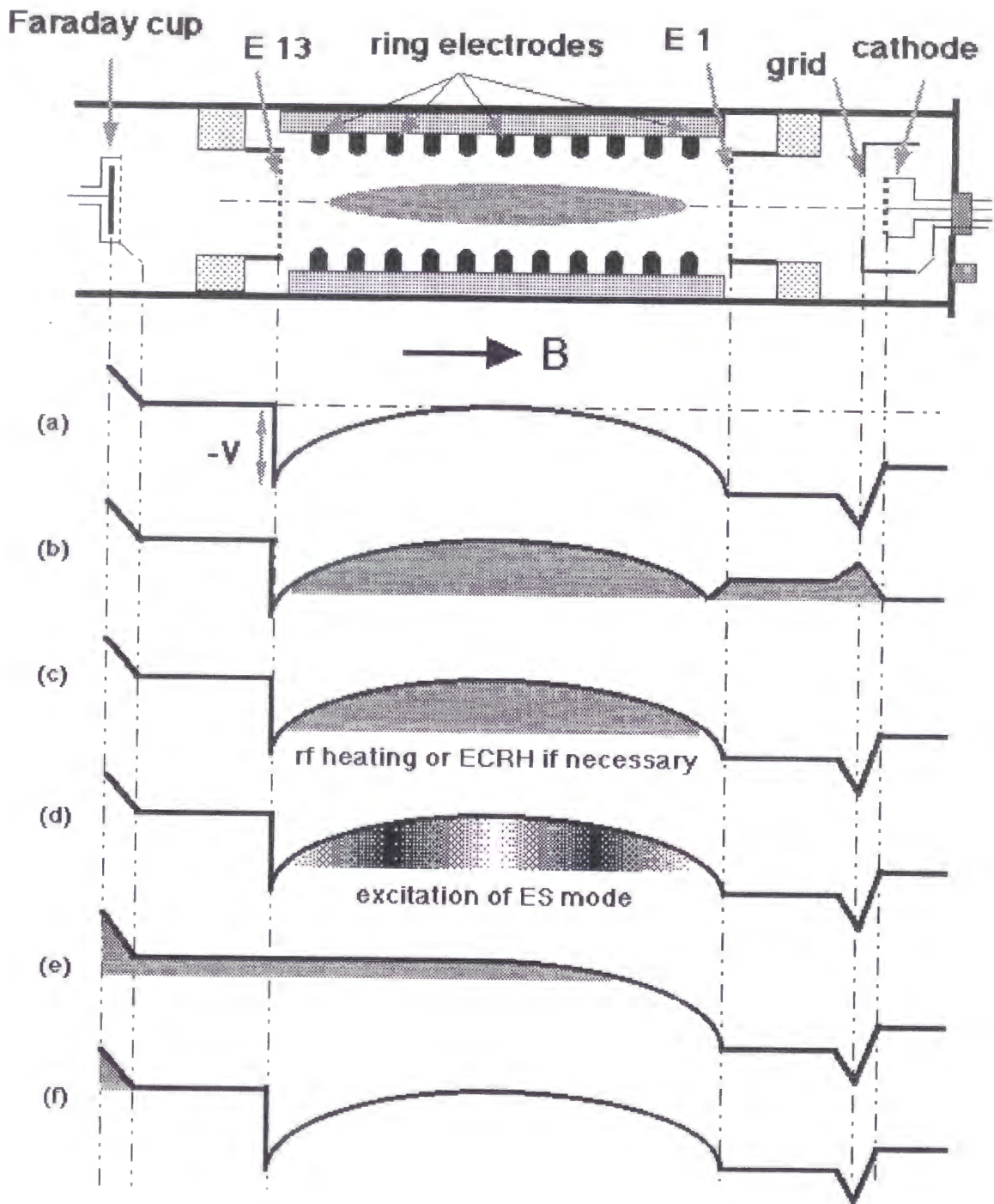
Figure 3.3: *The sequence of the potential control in the MRE trap.*
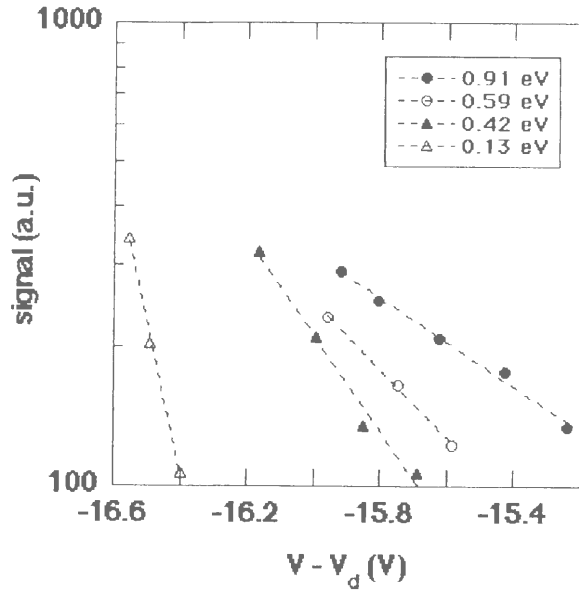
Figure 3.4: *Assuming the Maxwell distribution, the high energy tail of the distribution is used to determine the plasma temperature.*
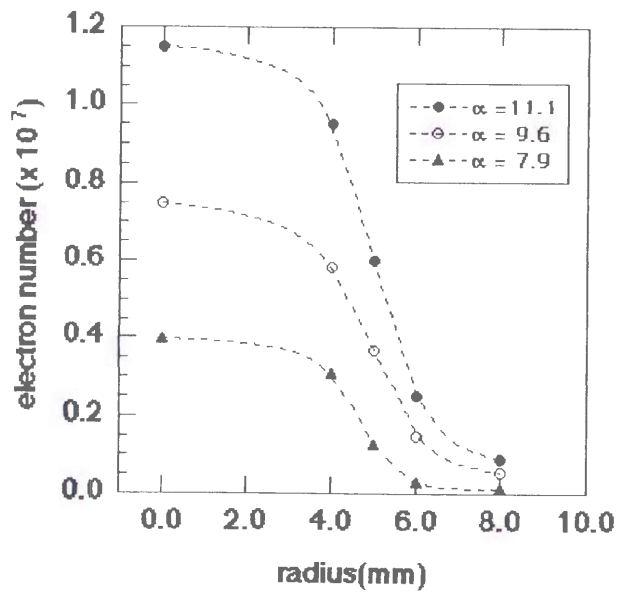
Figure 3.5: *The measured radial profile of the spheroidal plasma is used to determine α.*

to (α=11, ρ_p=7.5 mm), (α=9.6, ρ_p=7.5 mm) and (α=7.8, ρ_p=6.5 mm) with $T \sim 0.1$ eV. Open diamonds correspond to (α=11, ρ_p=7.5 mm) with $T \sim 1.5$ eV. For the plasmas in this examples, λ_D is estimated to be less than 0.11 cm at $T = 0.1$ eV and $\lambda_D < 0.33$ cm at $T = 1.5$ eV. Therefore, λ_D is smaller than ρ_p. Although λ_D may not small enough at high temperature, it can be seen that there is no noticeable change in the profile. Thus, the practical way to determine plasma parameters like α, ρ_p and z_p is to assume that a plasma has a constant density $n(\alpha)$ given by eq.(2.8). Then the equation

$$N_c \sim 2\pi r_c^2 n(\alpha)\alpha\rho_p(\alpha, N) \tag{3.1}$$

is solved to obtain α with the measured N and N_c. Here, N_c is the received charge by the segmented faraday cup on the axis. Once α is obtained, ρ_p and z_p are easily derived and it is confirmed that ρ_p is consistent with the measured radial profile.

Chapter 4

Diocotron oscillations

The linear diocotron oscillation in the multi-ring electrode trap is discussed in this chapter. The theoretical dispersion relations of diocotron oscillations are available only for a cylindrical plasma surrounded by a conducting wall and for a spheroidal plasma without a boundary. It is difficult to obtain a dispersion relation for a spheroidal plasma with a cylindrical boundary. However, it is easy to imagine that the dispersion relation for a spheroidal plasma with a cylindrical boundary should be approximated by the fomer ones. When a plasma has a large α, it can be regarded as a cylindrical plasma and it should be approximated by a spheroidal plasma when it has a small α and its image charge effect is negligible. This is easily confirmed by experiment. Although it is empirical one, we can establish a dispersion relation and it can be used as a nondestructive diagnostic of the plasma under a special condition.

4.1   Experiments and Discussion

A radius of a plasma ρ_p is almost constant for a different α since the cathode and the magnetic field are fixed. This means that α of a plasma is easily controlled by changing N with a fixed ρ_p. For the experiment described in this chapter, no heating is applied to exclude temperature effect as far as possible. The plasma temperature in this experiment is less than 0.1 eV. Since a density of a plasma is between $2 \sim 8 \times 10^6 cm^{-3}$ ($4 < \alpha < 11$) in this experiment, λ_D is less than 0.16 cm. Examples of measured radial profiles $n\ell(r)$ are shown in Fig.3.5. Since there is the extra field caused by the image charges induced on the wall, the plasma may not be perfectly spheroidal. However, the measured radial profiles show approximately the characteristic quadratic dependence on r. This means that the deformation of the plasma is not so large as far as α is less than 11, which is the largest α in this experiment. When N is increased further to obtain larger α, a plasma expand radially and α becomes smaller. This is regarded as an effect of image charges.

Diocotron oscillations of the lowest azimuthal mode, i.e. $m = 1$, were excited by applying small electrostatic perturbations for 2 ms to one of four sectors of No.7 electrode, where the perturbation frequency was chosen quite close or equal to the natural mode frequency f_d. After the cease of the excitation, f_d was measured from signals on another sector of No.7 electrode. Detected signals are shown in Fig.4.1. Figure 4.2 shows plots of f_d for different α's and their least square fitting curve ($f_d = 0.19 + 0.66\alpha (4 \leq \alpha \leq 12)$) given by solid line.

We shall compare the observed frequency f_d with the frequencies in the two extreme cases. If a spheroidal plasma is free from boundary, the mode is expressed as ($\ell = 1, m = 1$)

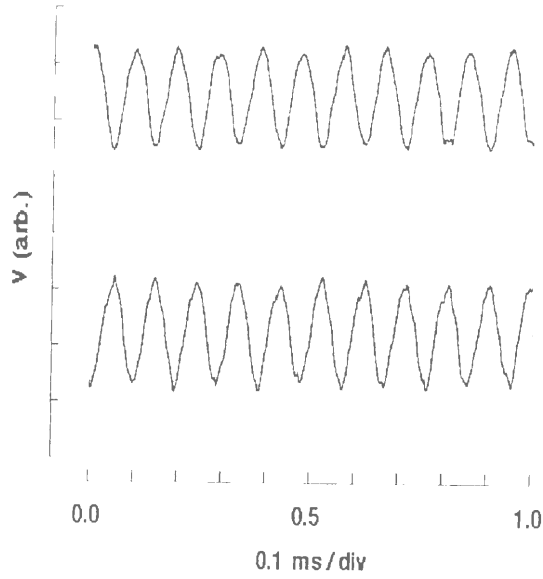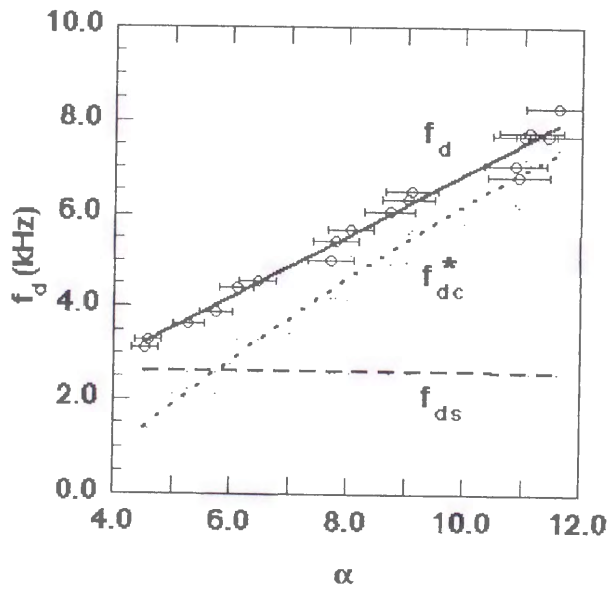Figure 4.1: *The signals of l = 1 diocotron oscillations detected at segmented electrodes No.4.*

Figure 4.2: *The measured f_d as a function of α. Also shown are the caluculation for the spheroidal plasma and the cylindrical plasma.*

34

and its frequency $f_{ds} = \omega_{ds}/2\pi$ is determined from the dispersion relation [50]

$$\omega_{ds} = \omega_r - \frac{\omega_p^2}{\Omega_c}\{1 - \frac{Q_1^{1'}(k_2)}{Q_1^1(k_2)\alpha(\alpha^2 - 1)^{1/2}}\}. \tag{4.1}$$

where Q_1^1 is the associated Legendre function and $k_2 = \alpha/(\alpha^2 - 1)^{1/2}$.

In the other extreme case such that the plasmoid has a considerably large aspect ratio and it can be regarded as an infinitely long cylindrical column with the radius ρ_p, then the $m = 1$ diocotron frequency denoted by $f_{dc} = \omega_{dc}/2\pi$ is given by [4]

$$\omega_{dc} = (\frac{\rho_p}{b})^2\omega_r \tag{4.2}$$

for the case $\omega_p \ll \Omega_c$ which is satisfied in this experiment.

The broken line in Fig.4.2 is a curve of f_{ds} given by eq.(4.1) with the measured values of α and $n(\alpha)$ (eq.(2.8)). In this experimental condition, f_{ds} is nearly constant around 2.6 kHz. Substitution of the experimentally obtained ρ_p and $n(\alpha)$ into eq.(4.2) also leads to a formal value of f_{dc}: f_{dc}^* which is a frequency when the column has the radius of ρ_p and the density of $n(\alpha)$. The curve of f_{dc}^* is shown by the dotted line in Fig.4.2. It is clearly seen that f_d approaches f_{dc}^* as α increases, while, as α becomes smaller, f_d parts from f_{dc}^* and gets close to f_{ds} . Plasmoids with small α were formed at small N since the potential well of the trap was kept the same through the experiment. Therefore, the results support that the dispersion relation governing the diocotron oscillations is reduced to eq.(4.1) at very small N where the image charge effects becomes negligible.

The dispersion relation for m=1 diocotron oscillations may be written in the form [25]

$$G(\alpha) = -\frac{2}{\omega_p(\alpha)^2}\{(\omega_d - \omega_r)^2 - (\Omega_c - 2\omega_r)(\omega_d - \omega_r)\}. \tag{4.3}$$

Here, $G(\alpha)$ is a geometrical factor depending on the shape of plasmoid. In the case of a
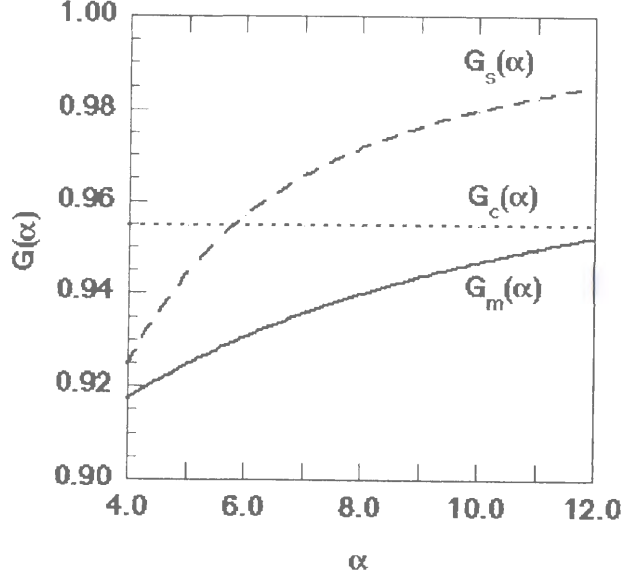
Figure 4.3: *Geometric factors determined by the measurement and by the dispersion relations for a spheroidal and a cylindrical plasma.*

spheroidal plasma being free from boundary, eq.(4.1) is rewritten to the form eq.(4.3) using

$$G(\alpha) \equiv G_s(\alpha) = 2/\{1 - \frac{Q_1^{1\prime}(k_2)}{Q_1^1(k_2)\alpha(\alpha^2 - 1)^{1/2}}\} \,, \qquad (4.4)$$

and for an infinitely long column with radius ρ_p located in the boundary wall of inner radius b

$$G(\alpha) \equiv G_c = 1 - (\frac{\rho_p}{b})^2 \,. \qquad (4.5)$$

The theoretical form of $G(\alpha)$ for a spheroidal plasma with boundary has not been found yet. However, $G(\alpha)$ can be evaluated numerically by substituting the experimentally obtained f_d (the least square fitting) and α in eq.(4.3) . Now, let this empirical factor be $G_m(\alpha)$. These three factors are drawn as a function of α in Fig.4.3. In this experiment, $\rho_p \sim$ 0.64 cm for $4 \leq \alpha \leq 12$ and then G_c (dotted line) is constant as 0.95. The solid line of $G_m(\alpha)$ approaches the broken line of $G_s(\alpha)$ as α (or N) decreases and, on the other

36

hand, $G_m(\alpha)$ comes near to the dotted line with increase in α. This behaviour of $G_m(\alpha)$ means as follows: the dispersion relation of $m = 1$ mode for a spheroidal plasma set inside a conducting wall is approximately expressed by eq.(4.2) given for a cylindrical column when α is large enough, and the relation becomes close to eq.(4.1) when N is so small that the image charge effect is negligible. Using the empirical $G_m(\alpha)$ in eq.(4.3), we can have the dispersion relation in an intermediate state between these extreme cases, but its application is not general and limited only to this experimental condition.

4.2 Summary

Diocotron $m = 1$ frequencies of spheroidal nonneutral electron plasmas, which were enclosed with a conducting wall and neither approximated as a cylindrical column nor as a spheroidal plasma with free boundary, were measured for a fairly wide range of α using the multi-ring electrodes trap. An example of the observed change in geometrical factor with α was also presented to see a variation of dispersion relation with α. If the relation of geometrical factor with α is generally found either theoretically or experimentally, the measurement of diocotron oscillations will offer a means of diagnosis of spheroidal plasmas, similarly to nondestructive measurements reported so far [17, 44, 45, 33].

Chapter 5

Electron plasma oscillations

The wall and temperrature effect on electron plasma oscillations of a spheroidal nonneutral electron plasma in the multi-ring electrode trap is discussed in this chapter. Although the temperature effect of the $l = 2$ mode when $T < 0.15$ eV was measured and compared with computer simulations, the results showed that the mode frequencies extrapolated to $T = 0$ deviated from those predicted by the Dubin's cold theory. It is thought that image charge effect caused these deviations. If image charge effect is included in a cold plasma, the temperature dependence of mode frequencies can be estimated by the change in the dielectric constant of the plasma. The measured mode frequencies of $l = 2$ and 3 up to $T \sim 1.5$ eV will be compared with values estimated by this method.

5.1   Experiments and Discussion

An example of the measured line integrated radial profile was shown in Fig.3.5. As described in section 3.2, eq.(3.1) is used to determine α and it is appropriate in the experimental condition. The rf heating was used to control a plasma temperature.

The cold theory predicts that the $l = 2$ mode has two mode frequencies $\omega_2^{\pm}$ ($\omega_2^+ > \omega_2^-$) and that ω_2^+ is comparable to Ω_c. In the experimental condition, $\Omega_c \sim$ 1.2×10^{10} rad/s, $\omega_p \sim 1.3 \times 10^8$ rad/s and $\omega_r \sim 8.0 \times 10^5$ rad/s. Then, the mode frequency in the range $\omega_r \ll \omega_2 \ll \Omega_c$ is ω_2^- to which eq.(2.42) is applicable. Hereafter only ω_2^- is examined so that the superscript (-) is omitted. This mode repeats radial expansion and contraction accompanied with axial contraction and expansion, keeping a constant density. Once parameters N, ρ_p, α are determined experimentally, the practical ω_2 is presumed to lie near the value estimated by eq.(2.42) . The applied rf perturbation frequency is tuned around it watching the amplitude of excited oscillations. After the perturbation, the natural $l = 2$ mode is again identified by observing phase relations among signals from different electrodes. The oscillatory signal of $l = 2$ mode from E4 is in phase to that from E10 but out of phase to that from E7, which is shown in Fig.5.1. Also signals from the four segments of E7 are all in phase because the mode is axisymmetric.

Mode $l = 3$ has two branches $\omega_3^{\pm}$ with the range of $\omega_r \ll \omega_3^- \leq \omega_z \leq \omega_3^+ \ll \Omega_c$. This experiment investigates ω_3^+ mode having no radial node. This mode can be excited by applying rf perturbation to an electrode. Hereafter the superscript(+) is omitted. In this case, two signals from E5 and E9 become out of phase and no oscillation signal can be detected by E7 because a node is on the midplane $z = 0$. The detected signals are shown in Fig.5.2.

A power spectrum of excited natural modes is shown in Fig.5.3. For demonstration, rf perturbations of three frequencies f_1, f_2 and f_3 ($f_1 < f_2 < f_3$) are simultaneously applied to different electrodes. Three peaks in Fig.5.3 correspond to the excited modes $l = 1, 2$ and 3, respectively.
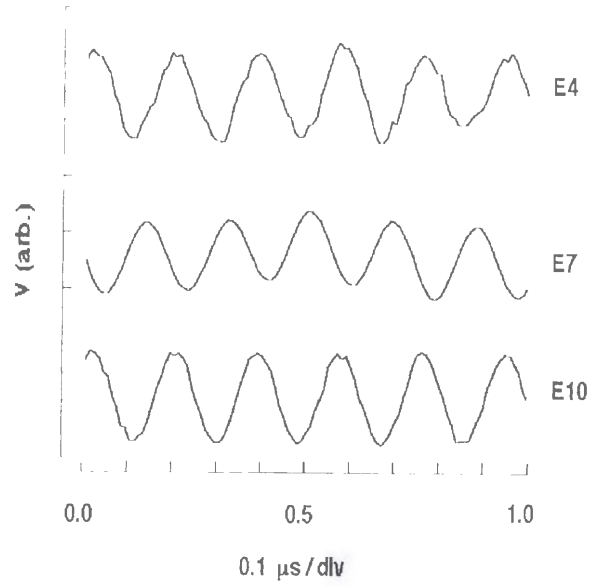
Figure 5.1: *The signals detected by electrodes E4, E7 and E10 of the axially symmetric electrostatic modes l = 2.*
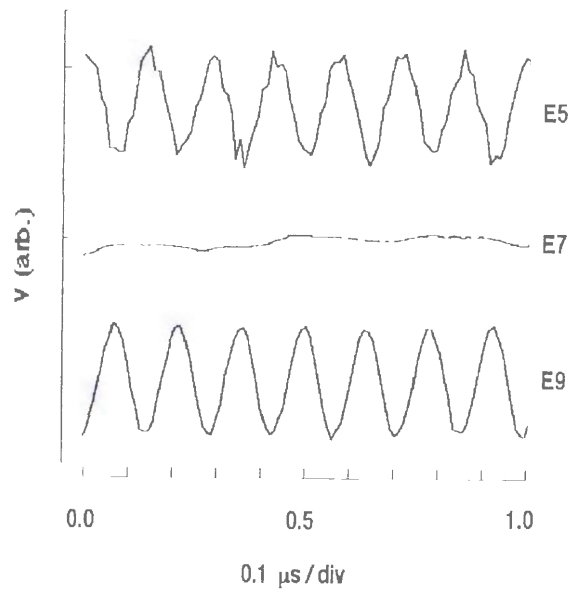
Figure 5.2: *The signals detected by electrodes E4, E7 and E10 of the axially symmetric electrostatic modes l = 3.*
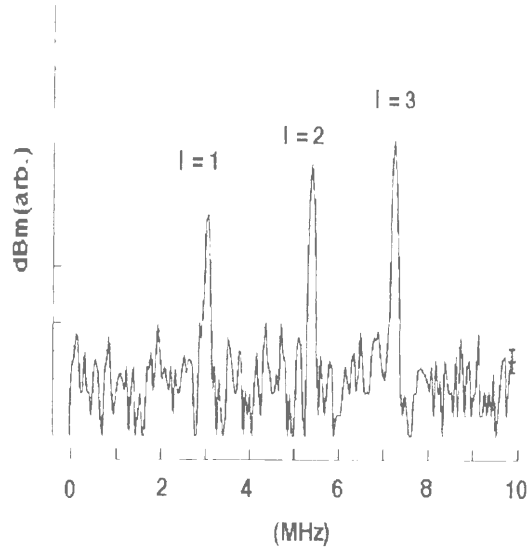
Figure 5.3: *The axially symmetric electrostatic modes of $l = 1, 2$ and 3 are excited simultaneously.*

5.1.1 Wall effects

The dispersion relation deduced for a cold spheroidal plasma does not include the effect of the conducting wall which surrounds the plasma. The nonneutral plasma induces image charges on the wall and they generate an additional electric field which acts on the plasma. Therefore, observed mode frequencies ω_l^{obs} may deviate from those found by eq.(2.42) ω_l^{cal}. In order to clarify such a boundary effect, it is important to determine the amount of the variation of observed frequency ω_l^{obs} with the increase of N by adjusting α to be constant. Although the equilibrium condition is slightly modified by the wall effect, it is considered that the density remains nearly constant, according to eq.(2.8). Since the plasma expands and approaches the conducting electrodes as N increases, it is expected that the wall effect causes more frequency shifts for a larger N.

11
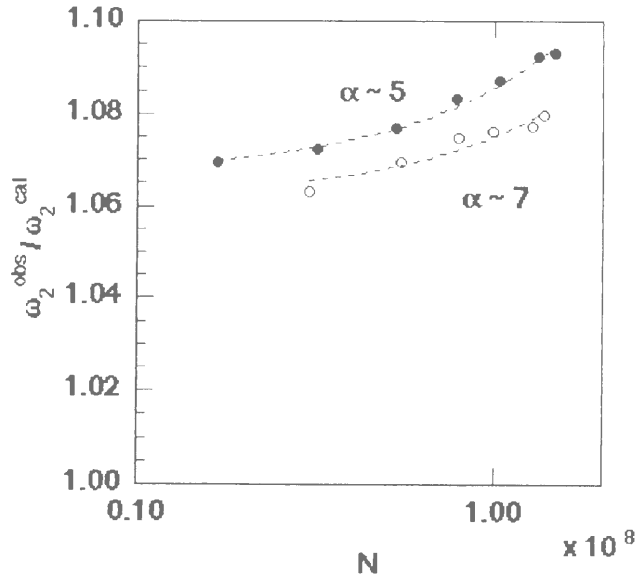
Figure 5.4: *N dependances of the ratio $\omega_2^{obs}/\omega_2^{cal}$ are measured for two cases $\alpha_c \sim 5$ and 7.*

Figure 5.4 shows experimentally obtained N dependances of the ratio $\omega_2^{obs}/\omega_2^{cal}$ for two cases as $\alpha \sim 5$ and 7, where $T \sim 0.03$ eV and the applied voltage is $V = -23$ V. Here, α is determined by the observed parameters N and N_c as mentioned earlier. The ratio $\omega_2^{obs}/\omega_2^{cal}$ becomes larger as N increases, i.e., the frequency shifts upwards with N. Errors included in the measured values lead to a 0.2% error in ω_2^{cal}, resulting in the error bars in Fig.5.4. The obtained results suggest that the boundary effect gives rise to a frequency shift. This situation will not alter essentially when the plasma is cold, because the fitting curves extrapolated to $T = 0$ in Fig.5.5, which shows another shift due to finite temperature, do not coincide with ω_2^{cal}. Similar frequency shift in the $l = 2$ case was observed and compared with particle simulation results [17]. The present experiment reconfirms this phenomenon and clarifies results by increasing only the total charge N at constant α.

As the exact dispersion relation, including the wall effect, has not yet been de-

termined theoretically, the observed frequency shift at $T < 0.03$ eV is denoted by $\delta\omega_2^{wall}$ through

$$\omega_2^{obs} = \omega_2^{cal} + \delta\omega_2^{wall}. \tag{5.1}$$

The plasma boundary in this experiment is diffusive due to collisions with residual gases. The change in the mode frequency caused by such a diffusive boundary is also included in the term $\delta\omega$. The frequency shift which is additionally caused by raising the plasma temperature will be considered with the term ω_2^{cal}.

5.1.2   Temperature effects

When the temperature of a spheroidal plasma becomes finite, its peripheral boundary is no longer sharp in density and becomes blunt even in the collisionless case. [49, 64] Also, its dielectric tensor itself becomes to depend on temperature.

Figure 5.5 shows observed temperature dependances of the mode frequencies of $l = 2$ and 3 at three different α's for $T > 0.15$ eV and $\rho_p \sim 0.7$ cm. The temperature is increased by applying the rf heating and α is the value for the case without the heating. Filled circles are measured at $\alpha \sim 7.9, N \sim 0.39 \times 10^8$ electrons, open triangles at $\alpha \sim 9.6, N \sim 1.0 \times 10^8$ electrons and filled squares at $\alpha \sim 11.1, N \sim 1.5 \times 10^8$ electrons. The angular frequencies ω_2^{obs} and ω_3^{obs} increase with T, becoming higher for smaller α at a same $T > 0.2$ eV. Similar temperature dependence in the case of $l = 2$ has been observed [17] and its approximate estimation was given by making use of one component compressive fluid model in the limit of high magnetic field. [17, 46] Here, a different method for estimating mode frequencies will be attempted and the estimated frequency shifts will be compared with the obtained results.
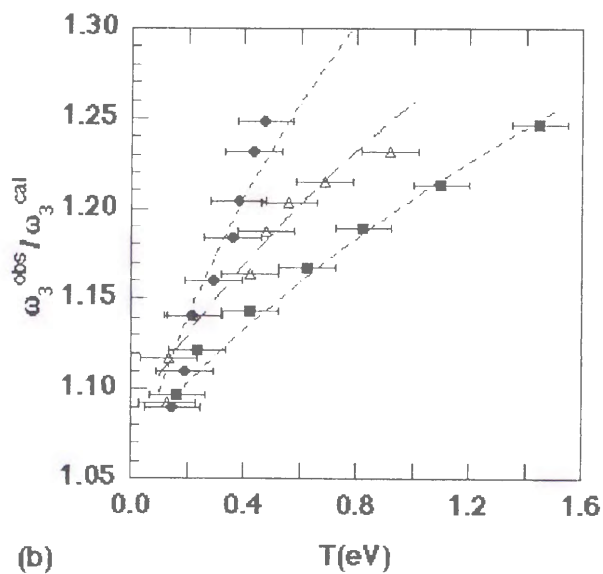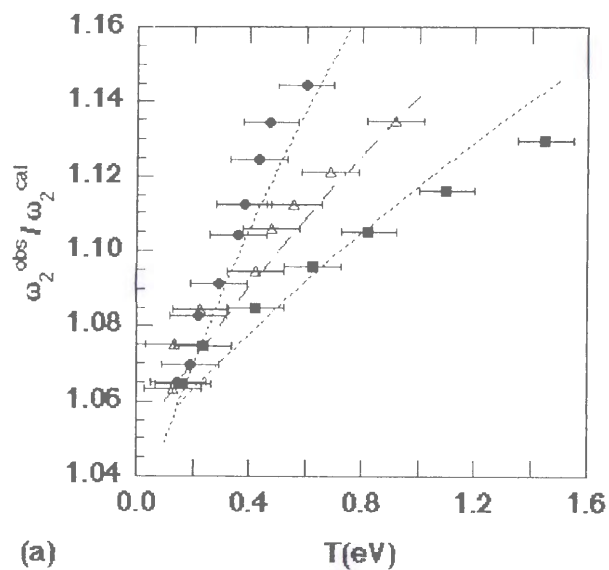
Figure 5.5: *The observed T dependance of the mode frequencies of l = 2 (a) and 3 (b) at three different α's for T > 0.15 eV and ρ_p ∼ 0.7 cm.*
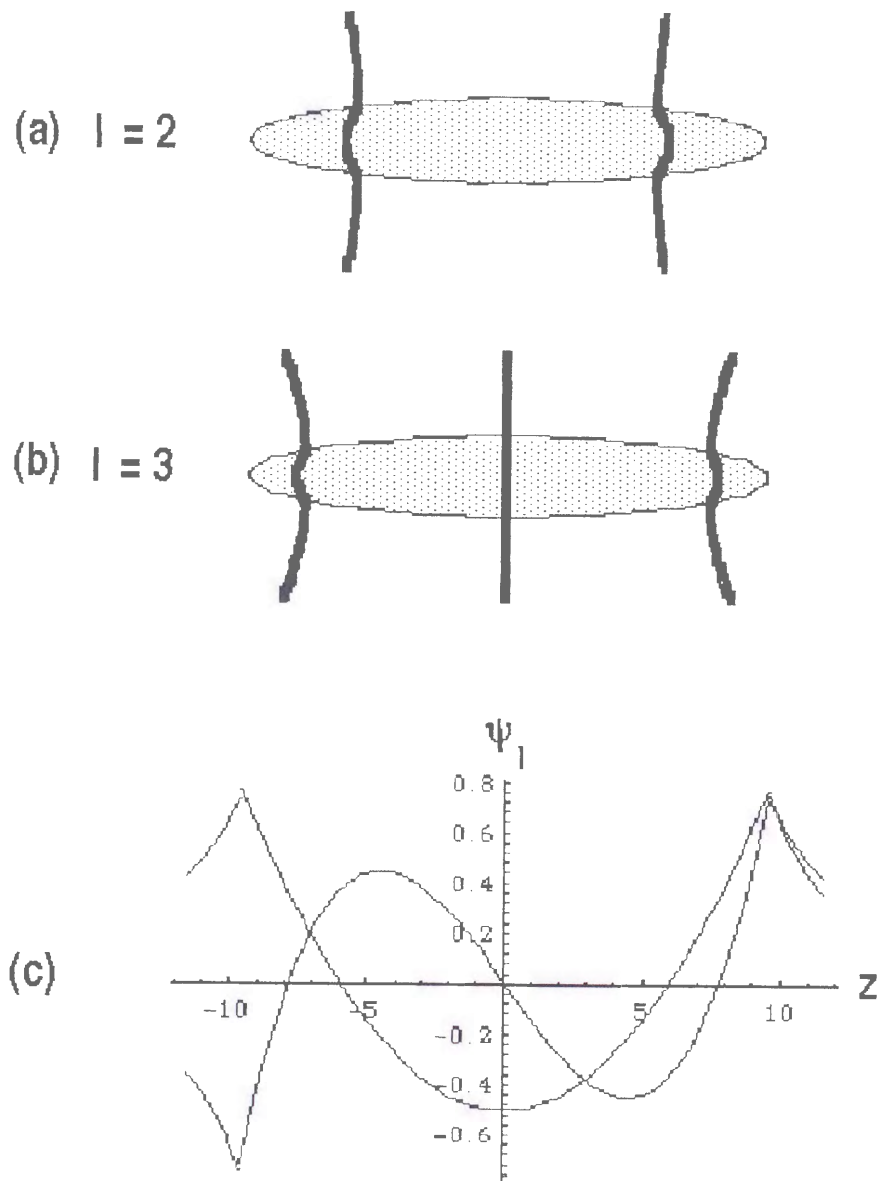
(a) l = 2

(b) l = 3

(c)

Figure 5.6: *The nodes of oscillations inside and outside of the spheroidal nonneutral plasma for l = 2 and 3.*

The observed modes ω_2 and ω_3 are axisymmetric and they have no node of oscillations in the radial direction. Figure 5.6 shows the nodes of these modes inside and outside of the plasma. The nodal surfaces are not planes but the axial wave length may be approximated as $\lambda_{zl} \sim 4z_p/(l-1)$ inside the plasma and also in the neighbouring vacuum region. Therefore, the corresponding wave number is $k_{zl} \sim \pi(l-1)/2z_p$. The bluntness of the plasma boundary due to finite temperature has been analysed and/or numerically examined [49, 64] and the results showed that it is a few times the Debye length. Since the largest Debye length λ_D in the experimental conditions is 0.33 cm at $T = 1.5$ eV, the depth of the bluntness is much shorter than the axial wave lengths of low order modes such as $l = 2$ and 3. The change in the net axial wave length λ_{zl} is less than 9% at temperatures up to 1.5 eV. In this experiment, therefore, $\lambda_D \ll z_p$ and λ_{zl} ($l = 2,3$) is not substantially changed by finite temperature. The temperature dependence of k_z is ignored in the following discussions.

When the plasma temperature is finite, the temperature dependence of the tensor element ϵ_3 in eq.(2.42) should be considered through

$$\epsilon_3 = 1 - \frac{\omega_p^2}{\omega^2}[1 + \frac{\kappa_B T}{m}(\frac{3k_\parallel^2}{\omega^2} - \frac{k_\perp^2}{\Omega^2})], \qquad (5.2)$$

where κ_B is Boltzmann constant, $k_\parallel = k_z$ and $k_\perp$ is the wave number perpendicular to the magnetic field. In this experiment, the term of $(k_\perp/\Omega)^2$ can be neglected to $(k_z/\omega)^2$ because $\omega^2 \ll \Omega^2$. Therefore, we have

$$\epsilon_3 = 1 - \frac{\omega_p^2}{\omega^2}(1 + \frac{\kappa_B T}{m}\frac{3k_\parallel^2}{\omega^2}). \qquad (5.3)$$

The temperature dependence of ϵ_1 is also negligible compared with that of ϵ_3. This is because the coefficient of the temperature dependent term becomes $O(\Omega_c^{-4})$. Since $k_z \sim$

46

constant, all components ϵ_3 and ϵ_1 are nearly constant inside the plasma. The analytical connection of the plasma region to the vacuum region becomes possible as in the research done by Dubin [50]. Thus, the dispersion relation of eq.(2.42) using ϵ_3 of eq.(5.3) will provide rough temperature dependence of mode frequencies, and the mode frequencies ω_l^{est} are expressed by adding the frequency shift due to the wall effects as

$$\omega_l^{est} = \omega_l(n, \alpha, T, k_z) + \delta\omega_l^{wall}. \tag{5.4}$$

The values of $\delta\omega_l^{wall}$ can be determined to be the difference between ω_l^{obs} at $T = 0.03$ eV and ω_l^{cal}. They are dependent on the plasma parameters as noted in the figure caption of Fig.5.4. Making use of these $\delta\omega_l^{wall}$ values, we can plot curves of ω_l^{est} on Fig.5.5. Although the measured quantities N and N_c include errors, these errors negligibly affect the calculated values of ω_l^{est}. Even if errors in T for ω_l^{obs} are taken into account, each curve is in substantial agreement with the corresponding observed plots. This means that the change of α with constant ρ_p is clearly detected in the multiring electrode trap. Here, deformation of the plasma shape from a spheroid which may be caused by the wall effects have not been taken into account because they are thought to be small in actuality, and the spatial density distribution has been assumed uniform although it is diffusive due to collisions with the residual gases. However, the agreement of ω_l^{est} with the observed mode frequencies suggest that the temperature dependence of a spheroidal plasma is mainly due to changes of the dielectric tensor and the other factors have little influence. Therefore, it is possible to use eq.(2.42) with eq.(5.3) and eq.(5.4) to estimate mode frequencies at lower temperature as long as $\lambda_D \ll z_p$ and λ_{zl}.

5.2   Summary

Electrostatic oscillations of spheroidal nonneutral electron plasmas in the multiring electrodes trap were investigated experimentally, and it was demonstrated that this trap is valid tool to studies of such an oscillation because the trap can confine a plasma with a large axial length and pick up the signals of many modes. By increasing N with a constant α, the observed upper shift of $l = 2$ mode frequency with N at room temperature proved to be primarily due to the wall effects.

Temperature effects on the changes in mode frequencies of $l = 2$ and 3 were observed in the range $0.03 < T < 1.5$ eV for fairly large α up to 11. The frequencies increased with T and the slopes became greater as α decreased in both cases of $l = 2$ and 3. It was possible to estimate this increase in the mode frequency with T by using the dispersion relation modified from Dubin's formula, where the dielectric constant was replaced with the general dielectric constant including finite temperature. Application of this method will be limited to low temperature cases so that the Debye length is sufficiently shorter than the size of the plasma and the dielectric tensor is approximately constant inside the plasma.

The wall effects on oscillations are characterized by the geometrical shape of the trap, so it is necessary to elucidate the effects for each type of a trap. In addition, it should be pointed out that the presence of the wall provides a harmful influence on the equilibrium in conjunction with plasma confinement. The multiring electrodes trap has the potential to cancel the influence on the equilibrium by imposing an appropriate potential distribution on the electrodes.

Chapter 6

Decay instability of Langmuir waves

In this chapter, the behaviour of nonlinear electron plasma oscillations (Langmuir waves) in a confined nonneutral electron plasma column is discussed. As mentioned in section 2.4, the presence of a boundary totally changes the dispersion relation of Langmuir waves. It causes novel nonlinear phenomena which are not predicted by the theory of unbounded neutral plasmas.

6.1 Experiments and Discussions

6.1.1 Linear oscillations

The measured linear dispersion relation of Langmuir waves in a confined nonneutral electron plasma with a cylindrical boundary is shown in Fig.6.1. In this case, the plasma density $n \sim 6.9 \times 10^6 cm^{-3}$ ($N \sim 4 \times 10^8$) and the plasma temperature $T \sim 0.2$ eV give the Debye length $\lambda_D \sim 0.13$cm and the electron plasma frequency $\omega_p \sim 148$ rad/sec (23.5 MHz). As mentioned in the section 2.4, the Trivelpiece-Gould dispersion relation is suitable
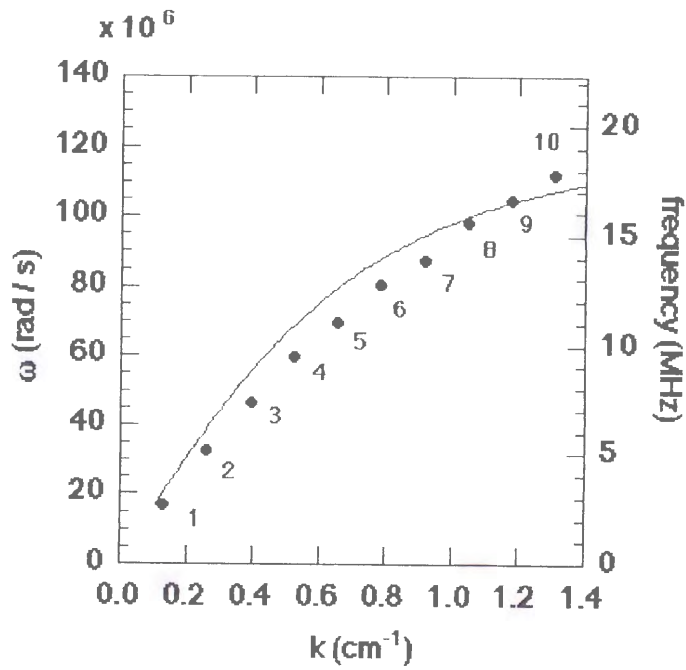
Figure 6.1: *The linear dispersion relation of the axially symmetric electron plasma waves in the axially confined nonneutral electron plasma column.*

for the present plasma [65]. It is seen that the oscillation frequency ω is proportional to k when k is small as a rough approximation. The solid line in Fig.6.1 is calculated from the Trivelpiece-Gould dispersion relation with the effective plasma density $n_{eff} \sim 5.0 \times 10^6 cm^{-3}$. The deviation from the measurement is mainly due to the density gradient in the radial direction. Observed Langmuir waves are standing waves and resonance frequencies become discreate in the long wave length region because the plasma is axially finite [5, 24, 66]. The electrostatic potential of these standing waves has antinodes at the ends of the plasma and the wave number k_ℓ of mode ℓ is approximately given by $k_\ell = \pi \ell / L$ where L is the axial length of the plasma [67]. Here, the approximate plasma length of $L \sim 24$ cm is used. This length is estimated by $\phi^{ex}(r, z)$ and the potential at which confined electrons begin to flow out from the confinement region.

The mode of oscillations can be identified by measuring the phase differences of detected signals. In the case of the mode $\ell = 1$, oscillations measured at $No.2 \sim 6$ have the same phase and those at $No.8 \sim 12$ have the antiphase. This means that the mode $\ell = 1$ has the only node at the center ($No.7$) electrode. In general, odd number modes have a node at the center electrode and they are neither excited nor detected with it. On the other hand, even number modes have an antinode at the center. In the case of $\ell = 2$, signals at $No.2 \sim 4$ and $10 \sim 12$ have the same phase and those at $No.5 \sim 9$ have antiphase. Thus it is seen that the mode $\ell = 2$ has two nodes. In general, the Langmuir wave of mode ℓ has ℓ nodes inside the plasma.

6.1.2   Nonlinear decay instability

It is seen from observations of linear oscillations that to excite a even mode oscilla-

51
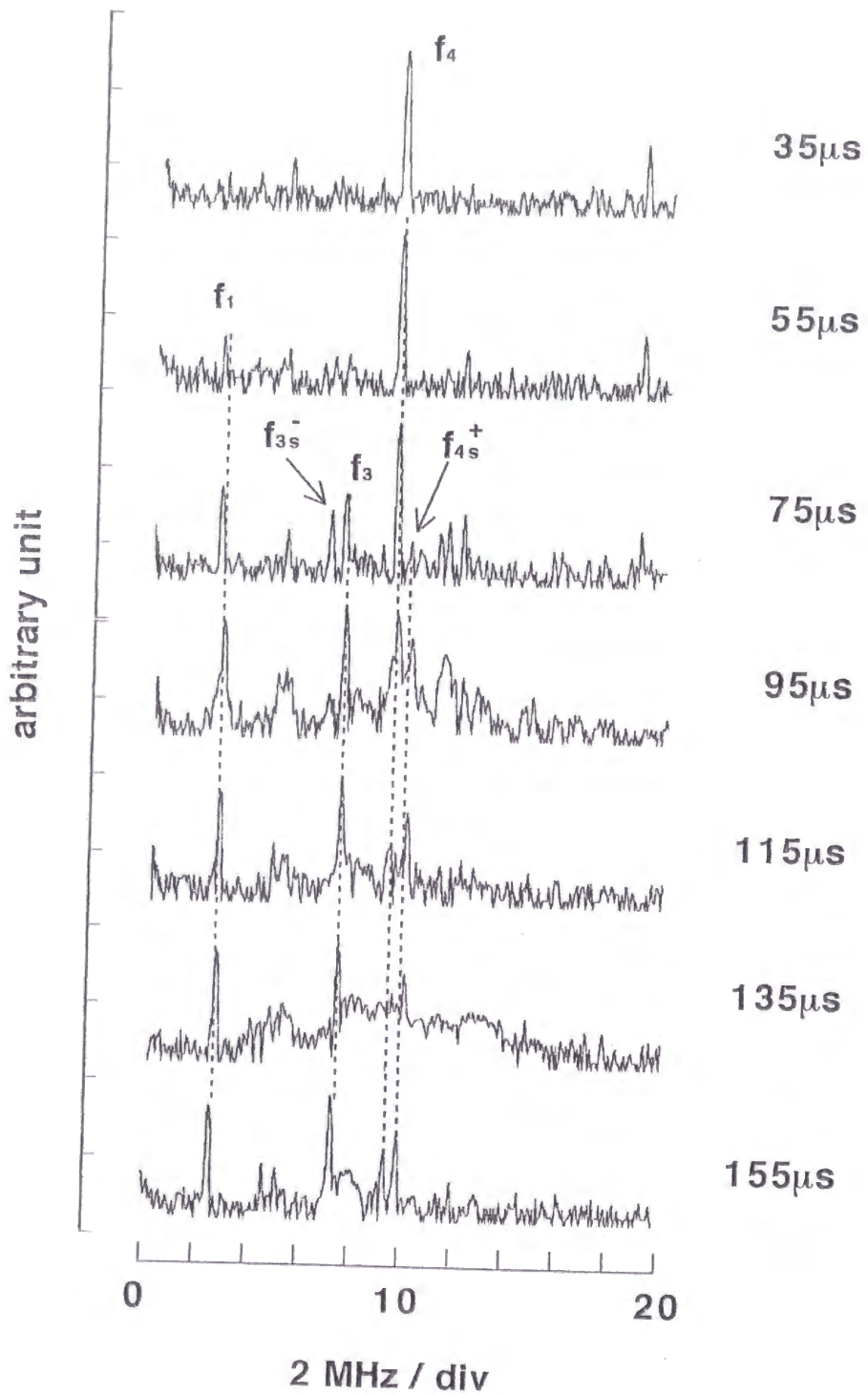
Figure 6.2: *The time sequence of FFT power spectrums of the signals, when a large amplitude Langmuir wave L_4 whose initial power is beyond the threshold is excited.*
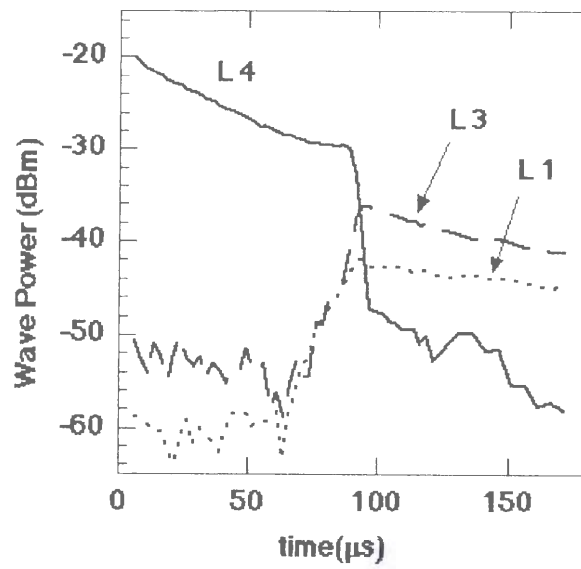
Figure 6.3: *It can be seen that the excited L_4 decays into L_1 and L_3 around $90\mu sec$.*
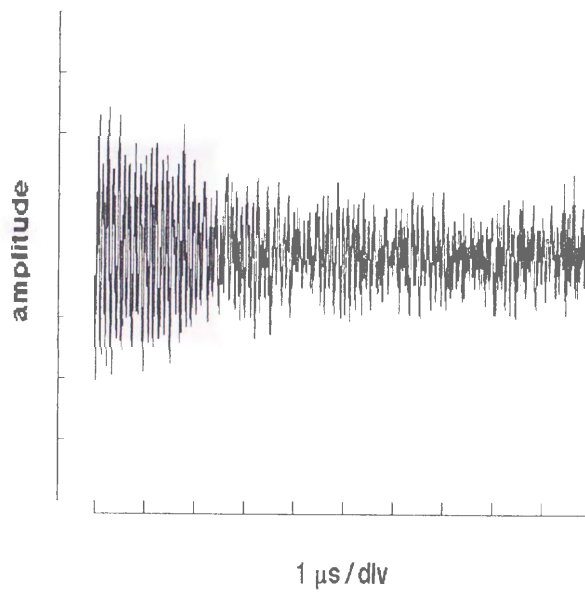

1 μs / div

Figure 6.4: *The decay instability is accompanied with the amplitude oscillation of Langmuir waves which causes a sideband instability and makes electron temperature higher.*

53

tion with the center electrode is the easiest way to excite a single large amplitude Langmuir wave. A typical behavior of a large amplitude Langmuir wave whose initial power is beyond the threshold is shown in Fig.6.2 and 6.3. Hereafter, the Langmuir wave of mode ℓ is represented by L_ℓ. In these figures, the large amplitude (-23.6 dBm detected at the electrode No.4) L_4 is excited with the center electrode by applying the RF perturbation of 9.5 MHz during $4\mu sec$. The plasma parameters are the same as those in Fig.6.1. Shown in Fig.6.2 are the time sequence of FFT power spectrums of the signals detected at the electrode No.4. In Fig.6.3, the power of the main three peaks ($\ell = 1, 3, 4$) in Fig.6.2 are plotted as functions of time. It can be seen from these figures that only the excited L_4 dominates the oscillation of the plasma and it decays exponentially until $70\mu sec$. Then L_1 and L_3 begin to grow exponentially from the noise level ($\leq$ -50 dBm) to the level of initially excited wave (-35 dBm) until $90\mu sec$. On the other hand, L_4 changes the decay rate suddenly at $90\mu sec$ and heavily decays from -30 dBm to -47 dBm until $100\mu sec$. As a result, L_4 decays and L_1 and L_3 are created through this process. This is thought to be the decay instability among Langmuir waves, because no other oscillations such as diocotron oscillations and electron cyclotron oscillations can be observed during this process and there is no ions which lead to low frequency ion sound waves.

The decay process described above occurs only when the power of the excited L_4 exceeds a certain level. When the initially excited Langmuir wave is below the threshold, it just decays away exponentially and no other wave is excited. This is because the mode frequencies of $f_1 = 2.6$ MHz, $f_3 = 7.4$ MHz and $f_4 = 9.5$ MHz do not satisfy the condition $\omega_4 = \omega_3 + \omega_1$. In the case of figure 6.2, the excited large amplitude Langmuir wave makes

sidebands of $f_{ls}^{\pm} = f_t \pm 0.5$ MHz to grow and these sidebands satisfy

$$\omega_4 = \omega_{3s}^{-} + \omega_1 \qquad and \qquad \omega_{4s}^{+} = \omega_3 + \omega_1. \qquad (6.1)$$

In fact, amplitude oscillation of Langmuir waves which causes sideband instability and makes electron temperature higher is sometimes detected by a ring electrode [57, 59]. The amplitude oscillation detected at $No.7$ electrode in this example is shown in Fig.6.4. The frequency of this amplitude oscillation is about 0.5 MHz. Therefore, the sideband instability associated with the large amplitude Langmuir wave is fundamental to these decay processes. One remarkable feature in this case is that the excited large amplitude L_4 which is above the threshold can not decay into other waves immediately unless they satisfy the energy conservation relation. Therefore, it can be said that it takes several tens μs for sidebands to grow. In this example, small peaks of $\ell = 2$ and 5 ($f_2 \sim 4.8$ MHz and $f_5 \sim 11.6$ MHz) can be seen during decay processes ($75\mu s$ and $95\mu s$). It suggests that the processes $\omega_4 = 2\omega_2$ and $2\omega_4 = \omega_3 + \omega_5$ occur at the same time. It is also seen that there is a peak at 19 MHz which is the second harmonic of f_4. Unfortunately it was difficult to exclude this harmonic entirely when a large amplitude f_4 was excited. It is possible to imagine a process like $2\omega_4 = \omega_3 + \omega_5$ contribute the process. However, the power of the second harmonic is not large enough to have a significant effect on the process. In addition to the energy conservation relation, the decay process must satisfy the momentum conservation $k_\ell = k_{\ell'} + k_{\ell''}$. In the case of Fig.6.2, $k_4 \sim k_3 + k_1(k_4 \sim 0.52, k_3 \sim 0.39, k_1 \sim 0.13)$ is satisfied. This implies that this process is basically a three wave process, i.e. L_4 decays into L_3 and L_1. Theoretically, 5 wave interaction is a higher order process compared with 3 or 4 wave interaction [61]. Thus, it can be ignored.

The process shown in Fig.6.2 is an example and does not mean that L_4 always

decays into L_1 and L_3. What kind of processes occur in a plasma depends on parameters such as a plasma density, initial amplitude and so on. If the plasma density is lower than that in Fig.6.2, it is observed that L_4 decays into L_2 and L_1. When the initial amplitude is larger than that of Fig.6.2, it is observed that L_4 decays into many other modes $L_1 \sim L_5$ (mainly into L_1). Furthermore, L_4 is not the only mode which causes these decay processes.

Another example of decay process is shown in Fig.6.5 and 6.6. In this case, large amplitude L_6 is excited at first. It is seen that L_6 decays exponentially while L_4 and L_8 grows exponentially until $50\mu sec$. Since, $f_4 = 9.3 \ MHz$, $f_6 = 12.8 \ MHz$, $f_8 = 16.3 \ MHz$ and $k_4 \sim 0.52, k_6 \sim 0.78, k_8 \sim 1.04$, this process satisfies

$$2\omega_6 = \omega_4 + \omega_8 \qquad and \qquad 2k_6 = k_4 + k_8. \tag{6.2}$$

This is the four wave process. Although clear sidebands are not observed, their frequencies are shifted from linear ones. Therefore, nonlinear frequency shifts are responsible for this process. Then a few sidebands such as $\omega_3^+ = 7.6 \ MHz$, $\omega_5^\pm = 11.0 \pm 0.3 \ MHz$, $\omega_8^- = 15.8 \ MHz$ appears and L_5 begins to grow abruptly. With these sidebands, the following interactions become possible. $\omega_6 + \omega_8^- = \omega_3 + \omega_4 + \omega_5^+, k_6 + k_8 \sim k_3 + k_4 + k_5$ and $\omega_6 + \omega_8 = \omega_3 + 2\omega_5^-, k_6 + k_8 \sim k_3 + 2k_5$. These nonlinear interactions cease at $65\mu sec$ and all excited Langmuir waves begin to decay. However, these are higher order interactions and not likely to occur. It is difficult to figure out these processes with the three wave or four wave interaction. The similar process is also observed when the larger amplitude L_4 is excited. The fact is that sidebands make the frequency differences of neighbouring modes almost equal and wave energy is transferred to lower modes. Since every oscillation modes are standing waves in this nonneutral electron plasma column, they have virtually zero momentum and total momentum is conserved in these processes. A weak turbulent

56
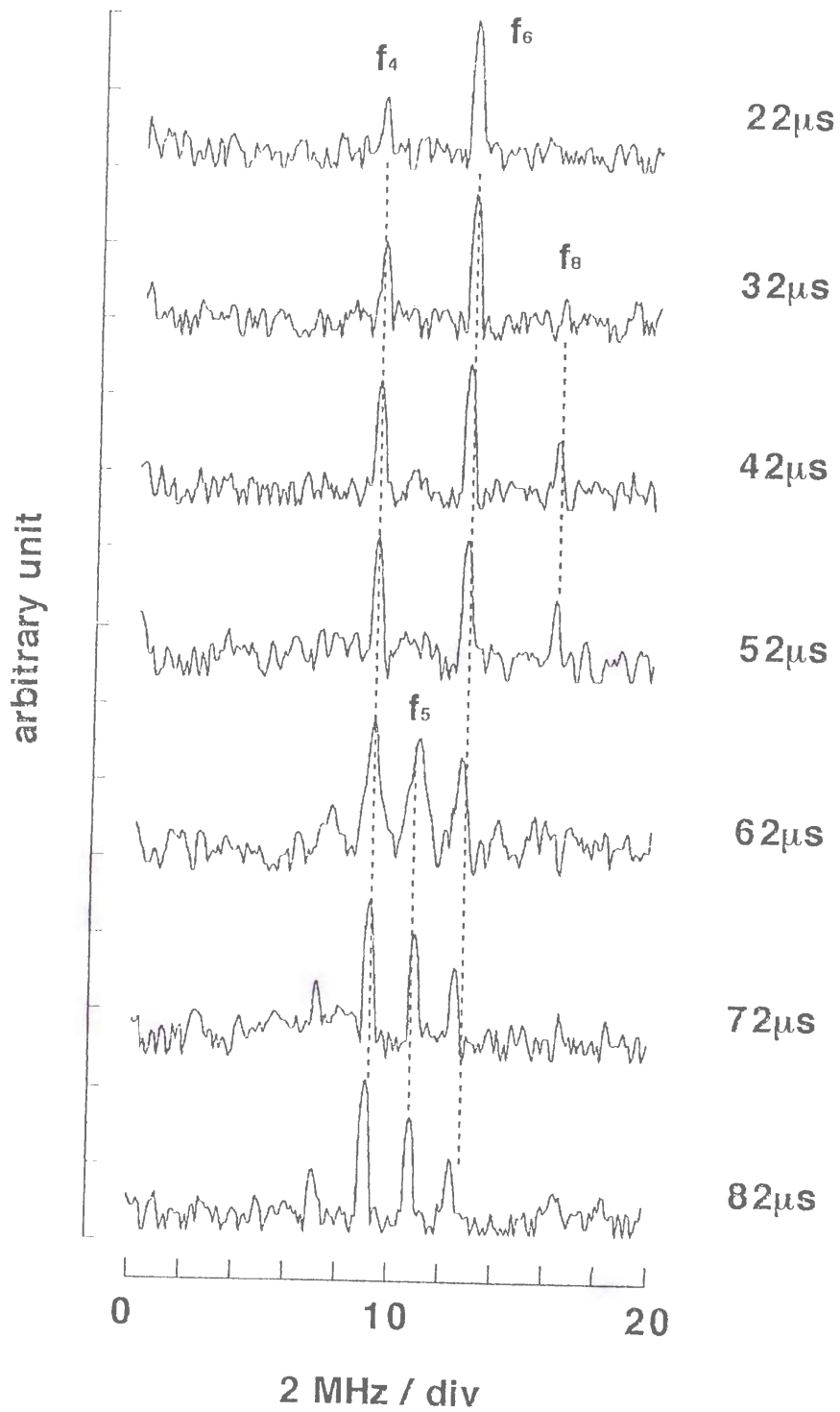
Figure 6.5: *The time sequence of FFT power spectrums of the signals, when a large amplitude Langmuir wave L_6 whose initial power is beyond the threshold is excited.*
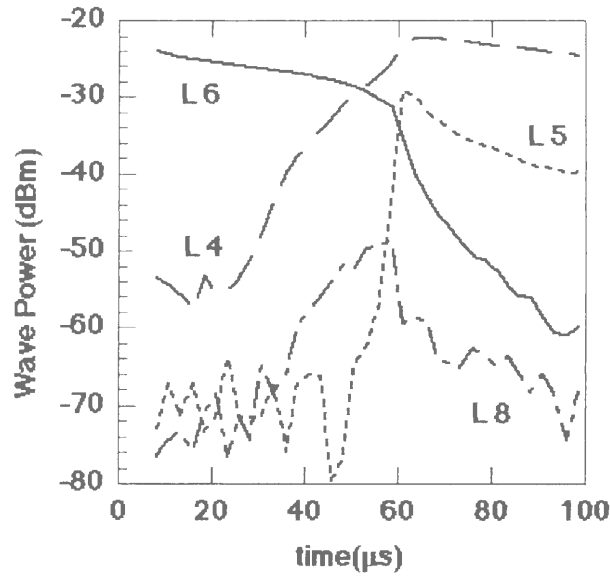
Figure 6.6: *It can be seen that the excited L_6 decays into L_4 and L_8 at first. Then L_5 is excited abruptly.*

state might be produced by the initial large amplitude Langmuir wave. If the dispersioin relation is regarded as continuous (at large ℓ) and the excitation period is optimized, the Kolmogorov spectrum might be obtained at large k. Since the present apparatus is not suitable for the measurement of short wave length, this problem is treated in the future.

As already mentioned, these decay processes have thresholds for the power of the initially excited wave. It is found that the threshold depends on the plasma temperature. Shown in Fig.6.7 is the case in which L_4 is initially excited. The abscissa is T in eV and the ordinate is the power of the initially excited Langmuir wave. Open circles mean that an initially excited L_4 does not decay into other waves and filled circles mean that L_4 decays into other waves. The obtained results show that the threshold becomes lower as the plasma temperature becomes higher. The temperature dependence of the threshold

Figure 6.7: *The temperature dependence of the threshold fits the exponential function* $\exp(-\alpha T)$ *with* $\alpha \sim 4$ *represented by the dotted line.*

fits the exponential function $\exp(-\alpha T)$ with $\alpha \sim 4$ represented by the dotted line. When T becomes higher, ω_f and Γ_f become larger. Thus the obtained result is contrary to the theory that threshold is proportional to $4\omega_{k'}\omega_{k''}\Gamma_{k'}\Gamma_{k''}$. It is thought that the propo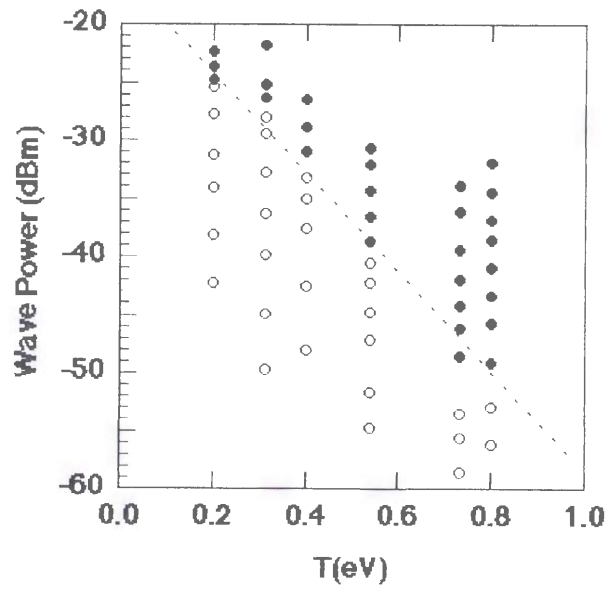rtional coefficient in this system depends on temperature or that the broadening of frequency spectra due to temperature causes this temperature dependence. However, the clear evidence for such a spectrum broadening was not found in the present observation.

6.2 Summary

The three wave and four wave decay instability of Langmuir waves were experimentally observed in nonneutral electron plasmas on the condition that the plasma had a finite axial extent with a cylindrical boundary. One remarkable feature is that the three wave process of Langmuir waves is possible in the plasma, which is forbidden in the unbounded neutral plasma. This is mainly due to the difference of dispersion relations. The energy conservation relation for a decay instability was satisfied by the presence of sidebands or nonlinear frequency shifts of mode frequencies. The absence of ion sound waves makes the measurement of the processes clear; a Langmuir wave can not decay into an ion sound wave and a Langmuir wave. It was also observed that the threshold power of the pump wave for the instability decreased exponentially as the plasma temperature became higher. Similar results should also be observed in a positron plasma and an ion nonneutral plasma.

Chapter 7

Conclusion

The main topic of this Doctor thesis are the linear and nonlinear electrostatic oscillations in the nonneutral electron plasma confined in the multi-ring electrodes (MRE) trap.

The dispersion relation for the fundamental diocotron oscillation of the spheroidal nonneutral electron plasma in the MRE trap was determined experimentally. The dispersion relation approaches asymptotically to the Dubin dispersion relation as the total electron number N or the total charge decreases (with small α), while it approaches to the dispersion relation deduced for an infinitely long cylindrical plasma column when N becomes larger (with large α). Therefore, the intermediate relation between the dispersion relation for the cylindrical plasma column and the Dubin dispersion relation was revealed out by the experiment. The empirically obtained dispersioin relation in this experiment can be used for the diagnosis of the plasma under the special condition. This is quite useful for antimatter plasmas in which destructive measurement is not favorable.

The wall and temperature effects on the electron plasma oscillations of the spheroidal

nonneutral electron plasma in the MRE trap were also studied. The frequency shifts caused by the wall effect were observed for the plasmas composed of $10^7 \sim 10^8$ electrons at room temperature. The temperature effect on mode frequencies was also measured up to 1.2 eV for both $l = 2$ and 3 modes. On the other hand, these frequencies are estimated by including the lowest order temperature effect of the plasma dielectric tensor in the dispersion relation and adding the frequency shifts measured at room temperature. The calculated results fit well with measured frequencies. This means that this simple calculational procedure is useful for evaluating the frequency shifts as far as Debye length is small compared with a plasma scale. These experiments made it clear that the conducting wall surrounding a spheroidal nonneutral plasma affects the characteristics of electrostatic oscillations when the total particle number is large.

The experiment with nonlinear Langmuir waves in the cylindrical nonneutral plasma was performed. It was found for the first time that a large amplitude Langmuir wave in a nonneutral electron plasma column decays into other modes of Langmuir waves when its amplitude exceeds a threshold. This nonlinear interaction is caused by formation of sidebands and nonlinear frequency shifts. There is a threshold for this nonlinear process and it becomes lower as the plasma temperature becomes higher. However, this temperature dependence is contrary to the theory for decay instabilities. Although three wave process among Langmuir waves is prohibited in the unbounded neutral plasma, this experiment proved that three wave interaction exists in the cylindrical nonneutral plasma of a finite length.

It should be noted here that the obtained results in this thesis have generality, i.e. they are applicable to every nonneutral plasma such as ion nonneutral plasmas, positron

plasmas. and so on. When a spheroidal nonneutral plasma which has a large number of particles is confined in a trap, the wall effect and temperature effect should be considered to evaluate a frequency of its electrostatic oscillations. When a nonlinear Langmuir wave is excited in a cylindrical or a spheroidal nonneutral plasma, it decays into other modes of Langmuir waves. This transition should be paid attention when we use the nondestructive measurement with electrostatic frequencies.

The Nobel prize for Wolfgang Paul and Hans G. Dehmelt in 1989 represents the Penning trap and Paul trap are the powerful tools for trapping fundamental charged particles in a vacuum. The long confinement time of the trap makes the precise spectroscopy of the trapped particles possible. Also the confinement of antiparticles $(e^+, \bar{p})$ became possible, that led to the measurement of CPT invariance with the higher precision. However, to make it progress further, i.e. to make a large number of $\bar{p} - He$, $p - p$ and anti-hydrogen particles for spectroscopy, it is desirable to confine much more e^+ and $\bar{p}$ at higher density so that they have larger cross sections. More efforts should be made to produce higher density nonneutral plasmas. Strongly coupled ion plasmas and dusty plasmas are studied with kinds of Penning traps, too. Since these traps are such useful tools, it is important to understand their properties much more. Further study in this field will open the way to the novel research with a large number of low energy antiparticles. I hope the works reported in this thesis can contribute in some degree to realize some features of these traps.

Appendix A

The etch rate acceleration by the ponderomotive force with the high intensity short pulse laser

All the results described in this chapter were obtained during my stay in the Department of Physics, University of Toronto as an exchange student.

The recent development of lasers with chirped pulse amplification (CPA) technique has extended its field of research drastically [68]. The high intensity ultrafast laser pulse created with CPA system has been widely used to study laser-plasma interactions for coherent X-ray generation, higher harmonic generation, inertial confinement fusion, etc [69]. However, the maximum intensity available with present laser systems is limited by the damage threshold of transparent materials. Since fused silica (SiO_2) is important optical components, its damage threshold has been studied [70, 71, 72]. Also, the controlled etching of materials like Si and SiO_2 has been an important issues for it has potential

applications for industries. Nevertheless, the etch rate of SiO_2 are investigated only with low fluences near the damage threshold until now. Since how an ultrafast laser pulse creates a plasma inside a material, how the laser produced plasma evolves, and how the laser pulse interact with the plasma are all important to be understood, the ionization process of SiO_2 interacting with ultrafast laser pulses was studied by some researchers. The velocity of the ionization wave was explained by standard electron thermal conduction at low intensity ($\leq 10^{15} W/cm^2$) [73, 74] and by radiative thermal conduction at high intensity ($\sim 10^{17} W/cm^2$) [75]. It is inferred that there is a transition of heat transport mechanisms in the range of the laser intensity between 10^{14} to $10^{17} W/cm^2$. These situations motivated us to investigate the etch rate of SiO_2 with a high intensity short pulse laser.

A.1   The experimental setup

The CPA laser system used in this experiment [76] has a feedbackcontrolled active/passive modelocked Nd:glass oscillator which can produce high-contrast picosecond pulses of microjoule energy at 1.054 μm wave length. These pulses are temporally stretched to 300 ps with a diffraction grating dispersive line. A selected pulse is optically amplified and finally recompressed by a grating pair compressor which is complementary to the stretcher. Changing the distance between the compressor gratings, various pulse durations (1.2 $\sim$ 32 ps) can be obtained with the maximum energy $\sim$ 800 mJ. A 300 ps pulse is also available by bypassing these compressor gratings. In the experiment described here, the energy of the laser ranges from 0.02 $\sim$ 400 mJ. The energy of the final output laser pulse is measured with a photo diode which was calibrated with an energy meter (morectron) in advance. In the last stage, the amplified pulse with 25mm diameter is focused with the lens
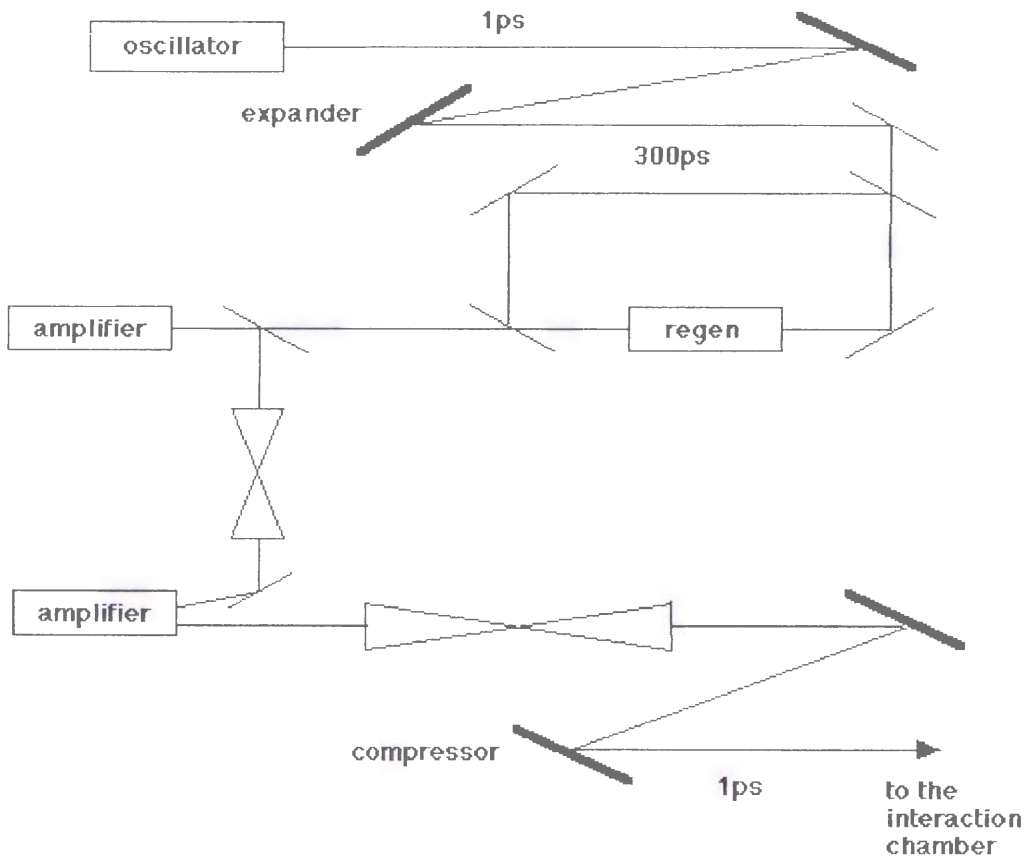
Figure A.1: *The schematic drawing of the CPA laser system.*

(f = 17 cm) attached to the vacuum chamber. The maximum energy corresponds to the maximum intensity of about $10^{17} W/cm^2$ with the focal spot size of about 300 μm^2 in the case of 1.2 ps pulse. The focused spot sizes of the laser for each pulse duration were imaged and calibrated with a x10 microscope objective and a CCD camera. The polarization of the final output can be easily changed between s- and p-polarization by placing a l/2 plate. The schematic drawing of the system is shown in Fig.A.1.

SiO_2 targets (1 x 1 inch) with thickness $\sim$ 200 μm (Corning 9695) were used in a series of experiments. The target is shot in the vacuum of $\sim 1 \times 10^{-2}$ torr with an incident angle of $\sim 15°$ or $\sim 35°$ and moved for each shot so that a focused laser pulse can

66

interact with a clean surface of a target. Since the fluence of the laser in this experiment are basically above the damage threshold of SiO_2 for each pulse duration, a depth of an etched hole can be measured with the stylus profiler (tencor alpha-step 200) whose vertical resolution is about 10 nm in our case.

The spectrum of the specularly reflected laser light at the incident angle of 35° is also measured with the spectrometer (American Holographic) whose resolution is 0.1nm in wave length. For this measurement, a pair of lenses (f = 14 cm) are set up to collect the reflected light effectively and to make it focus on the slit of the spectrometer.

A.2   Experiments and Discussions

As mentioned early in this chapter, the velocity of the ionization wave in SiO_2 could be well explained by standard electron thermal conduction at low intensity regime $< 5 \times 10^{14} W/cm^2$. This was experimentally confirmed with the pump-probe scheme. It was also found that the velocity of the ionization wave is consistent with radiative thermal conduction at a high intensity of $10^{17} W/cm^2$. In this case, the pump-probe scheme in a slightly different way was used for the experiment. Thus, there should be a transition from electron thermal transport to radiative thermal transport as the intensity of short pulse increases from 10^{14} to $10^{17} W/cm^2$.

Although measuring the depths of the etched holes gives only indirect information of the position and velocity of the ionization front, the obtained results for 1ps pulse shows the abrupt increase in the etch rate at high intensity. In Fig.A.2(a), solid circles mean the etched holes were made by 1ps pulse without the dye cell pulse cleaner and open circles mean the clean 1ps pulse were used. Although the clean pulse tends to have smaller etch
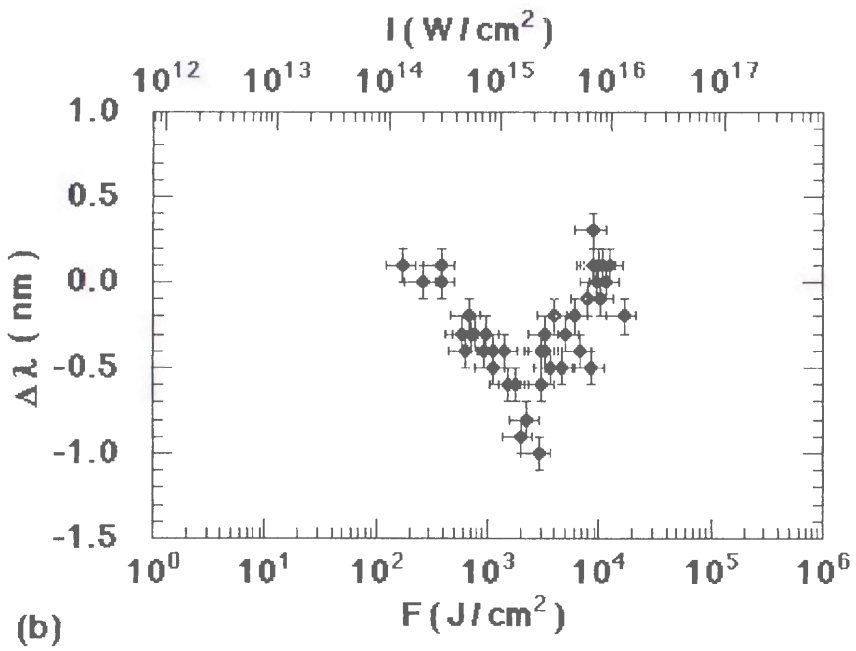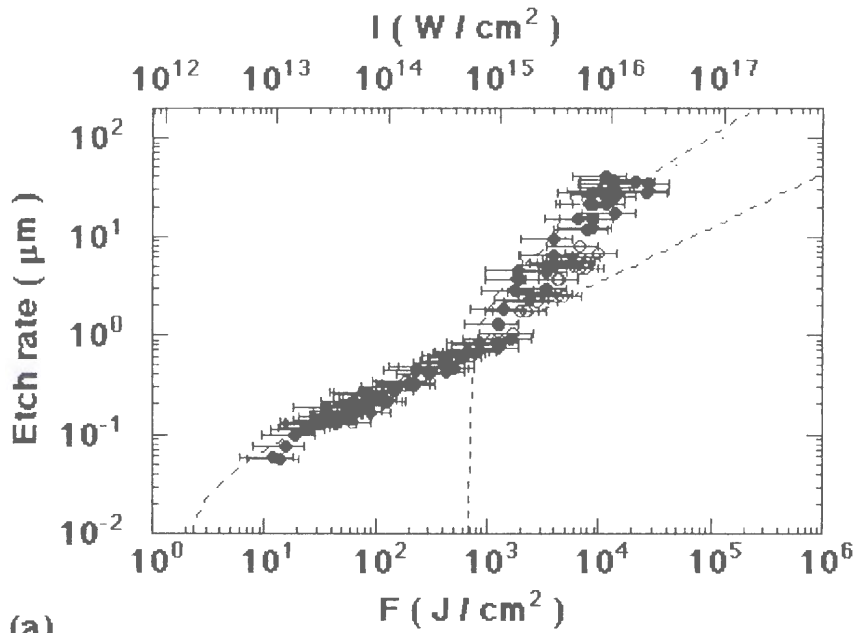
Figure A.2: *The etch rate of SiO_2 at various fluences for a 1ps laser pulse. (b) The wave length shift of the specularly reflected laser light.*

rate, it also shows the acceleration of the etch rate comparable to the dirty pulse. Even if the prepulse or pedestal of the 1ps pulse may enhance the acceleration of the etch rate, they are not the main reasons for the accelerated etching. The result shown in Fig.A.2(a) is explained using one dimensional thermal conduction inside a material, which is governed by the following equation

$$\frac{3}{2}n_e k_B \frac{\partial T_e}{\partial t} = \frac{\partial}{\partial x}\left[\kappa(T_e)\frac{\partial T_e}{\partial x}\right] \tag{A.1}$$

with Spitzer-Harm conductivity $\kappa_{SH} = 4k_B(k_B T_e)^{5/2}/m_e^{1/2}(Z+1)e^4 ln\Lambda$ for the electron thermal conduction [77]. Here, Z is the charge of the ion and $ln\Lambda$ is the Coulomb logarithm. In this case, the position of the ionization front is given by

$$x^{SH} = (\frac{8}{3m_e^{1/2}(Z+1)e^4 n_e^{7/2} ln\Lambda})^{2/9} F_{abs}^{5/9} t^{2/9}. \tag{A.2}$$

F_{abs} is the absorbed laser fluence. It is clear that the etch rates at low fluence $< 10^{15} W/cm^2$ are proportional to $\sim (F-2)^{5/9}$. Therefore, it reproduces the fact that the electron thermal conduction is the heat transport mechanism at a low intensity. However, the etch rate increases suddenly at $10^{15} W/cm^2$ and deviates from the fitting curve. At this higher intensity, radiative thermal conductivity $\kappa_{rad} = 16\sigma T_e^3 \lambda_R/3$ can be used for estimating the position of the heat front with eq.(A.1), which is expressed by

$$x^{rad} = 0.76(\frac{32\sigma}{9n_e^7 k_B^6 Z}9 \times 10^6)^{1/7} F_{abs}^{5/7} t^{1/7}. \tag{A.3}$$

Here, σ is the Stefan-Boltzman constant. The etch rates can be fitted by the function $\sim (F - I_{th})^{5/7}$ with $I_{th} \sim 10^{15} W/cm^{-2}$.

The measured Doppler shift of the specularly reflected laser light clearly suggests that the ponderomotive force [78] causes the accelerated etching as shown in Fig.A.2 (b). When the intensity is less than $\sim 10^{15} W/cm^{-2}$ and the pressure of the plasma expansion

dominates that of the laser electric field, the wave length of the reflected light shows the blue shift. The shift of the wave length becomes larger as the intensity becomes higher. This means the critical density surface moves out from the target and the velocity of the surface increases as the intensity increases. The expansion velocity v is easily estimated by the simple relation $\Delta\lambda/\lambda = -2(v/c)cos\theta$ with the incident angle θ. When the intensity is larger than $\sim 10^{15}W/cm^{-2}$, the ponderomotive force dominates the plasma pressure and the shift becomes smaller as the intensity increases. This is clearly seen in Fig.A.2 (b). It means that the expansion of the critical surface is suppressed by the ponderomotive force and the high temperature plasma stays longer on the surface of the target during the pulse duration providing the heat which is necessary for the onset of the radiative thermal conduction. A similar accelerated etching is observed for various pulse duration (3, 9, 30ps) with different threshold intensities.

However, a distinctive result is obtained for 300ps pulse as shown in Fig.A.3 (a) and (b). Although the etch rate shows a slight increase at $5\times10^{13}W/cm^{-2}$ with the red shift of the reflected laser light, the etch rate basically follows the electron thermal conduction for the entire range of the intensity. At low intensity, the cold temperature ($\sim$ a few tens electron volts) of the plasma eliminate the red shift caused by the Brillouin scattering [79] (The Brillouin scattering here means the process in which the incident laser light decays into the ion acoustic wave and the reflected light. When the plasma temperature is low, the low frequency of the ion acoustic wave leads to the small frequency shift of the reflected light). This explains the fact that there is no clear shift of the wave length at low intensity. At high intensity, the critical surface is pushed into the target by the ponderomotive force, which makes the plasma temperature higher, and the Brillouin scattering dominates the

interaction between the laser pulse and the expanding plasma [80], which results in the red shift of the reflected light. The fact that the etch rate at high intensity for 300 ps obeys electron thermal conduction law may be explained as follows. The scale length and density profile of the freely expanding plasma are given by $L_s = c_s t$ and $n = n_0 \exp(-x/c_s t)$ [69] respectively with $c_s = \sqrt{Z k_B T_e / M}$ the ion sound velocity and n_0 the density at the distance $x = 0$. Since 300 ps pulse has 300 times longer leading edge compared with 1 ps pulse, the preformed underdense plasma has 300 times longer scale length if the plasma temperature is the same for both 300 and 1 ps pulse. Although assuming the same temperature is inadequate, it is plausible to assume $10 \sim 30$ times longer L_s for 300 ps pulse. There is a huge difference in the amount of underdense plasmas which absorb the energy of the incoming laser when the peak of the laser pulse come into the target surface. Thus, the much longer scale length of the plasma prevents the effective heat deposition into the target and the onset of the radiative thermal conduction.

The condition that the ponderomotive force equals to the thermal energy of the electrons is given by [78]

$$ m < v_{os}^2 > /2 k_B T_e = 3.2 \times 10^{-13} I_{inc} \lambda_0^2 / k_B T_e \sim 1 \qquad (A.4) $$

with $v_{os} = eE/m\omega$. Thus, the electron temperature at the onset of the radiative thermal conduction can be estimated for each pulse duration as shown in Fig.A.4. Unfortunately no measurement was done to confirm the electron plasma temperature. However, obtained values are proper ones for this type of plasma. The empirical fitting $I_{th}(\times 10^{14} W/cm^2) \sim 13 \tau_p^{-1.44}(ps)$ is obtained for the threshold intensity of the accelerated etching from Fig.A.4.
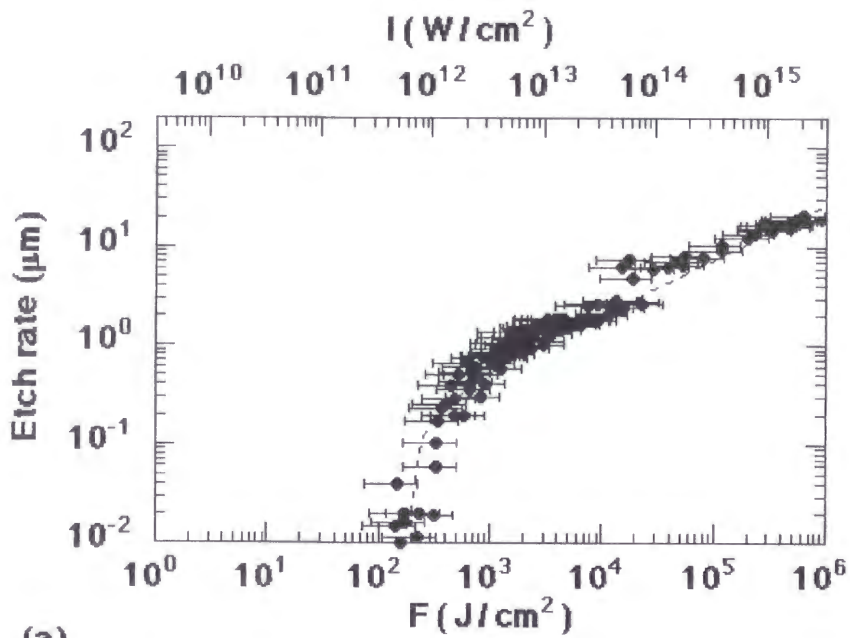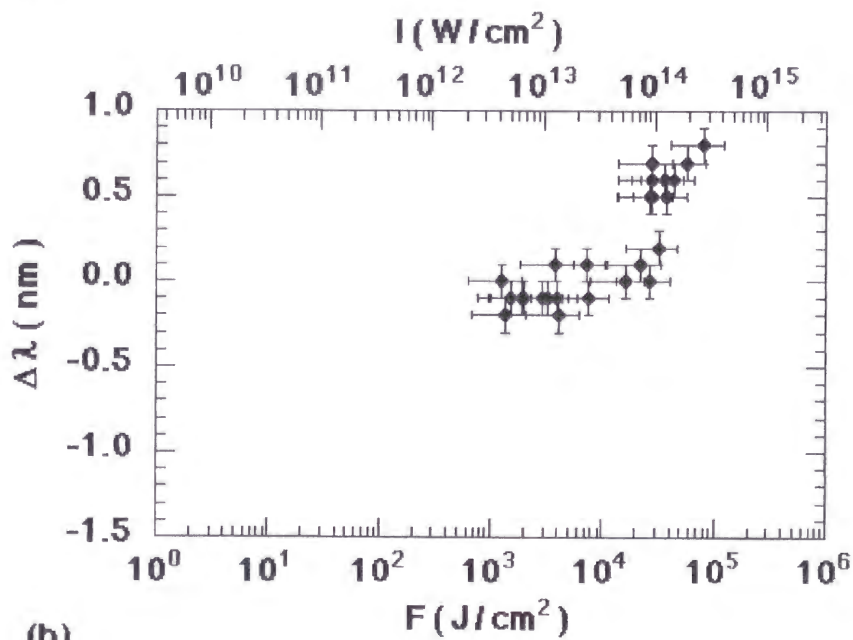
Figure A.3: *The etch rate of SiO_2 at various fluences for 300ps laser pulse. (b) The wave length shift of the specularly reflected laser light.*
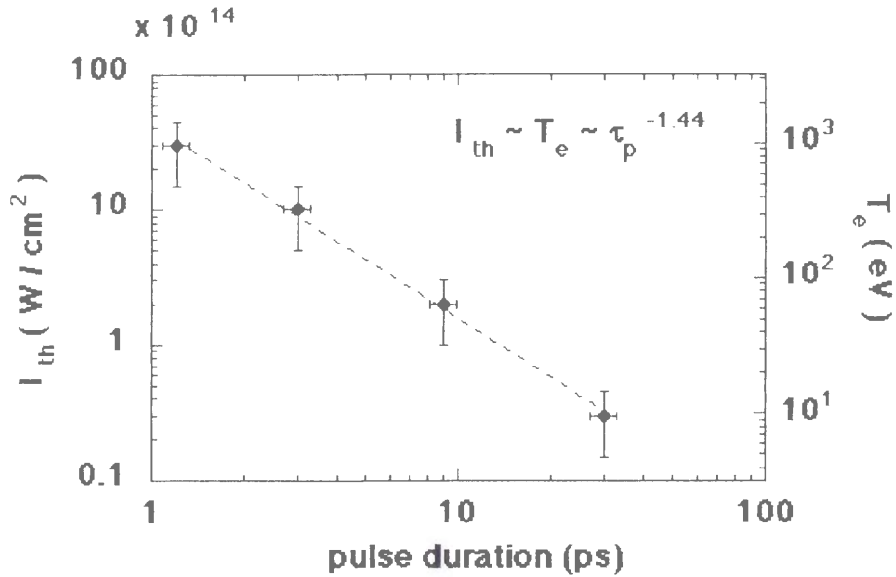
Figure A.4: *The threshold intensity for the accelerated etching depends on the laser pulse duration. The plasma temperature at the threshold is inferred by simple estimation.*

A.3 Summary

The interaction of an ultrafast high intensity laser with a solid surface of fused silica (SiO_2) was investigated. Measuring depth of holes etched by a laser pulse which has a broad range of intensity ($10^{13} \sim 3 \times 10^{16} W/cm^2$), a transition of thermal conduction mechanisms were clearly observed. For 1ps pulse, the etch rate follows the power law $\sim I^{5/9}$ in the low intensity range $\leq 10^{15} W/cm^2$, which is characteristic to the electron thermal conduction. However, the deviation from the power law with much higher etch rates indicates that the radiative thermal conduction dominates in the high intensity range $\geq 10^{15} W/cm^2$. The similar acceleration of the etching was confirmed for other pulse duration (3, 9, 30ps). By measuring the spectrum of the reflected laser light, it was found that the ponderomotive force plays an important role for the etch rate acceleration. In the case of

300ps pulse, however, this effect is suppressed by the longer scale length of the plasma.

The etch rate is basically determined by the electron thermal conduction.

Bibliography

[1] R. C. Davidson and N .A. Krall: Phys. Rev. Lett. **22** (1969) 833.

[2] R. C. Davidson and N .A. Krall: Phys. Fluids **13** (1970) 1543.

[3] R. C. Davidson: Theory of Nonneutral Plasmas (Addison-Wesley, Massachusetts, 1974)

[4] R. C. Davidson: Physics of Nonneutral Plasmas (Addison-Wesley, Massachusetts, 1990)

[5] J. H. Malmberg and J. S. deGrassie: Phys. Rev. Lett. **35** (1975) 577.

[6] J. S. deGrassie and J. H. Malmberg: Phys. Fluids **23** (1980) 63.

[7] C. W. Roberson and C. F. Driscoll: Nonneutral Plasma Physics, AIP Conference Proceedings No.175 (AIP, NewYork, 1988)

[8] J. H. Fajans and D. H. E. Dubin: Nonneutral Plasma Physics II, AIP Conference Proceedings No.175 (AIP, NewYork, 1995)

[9] J. H. Malmberg and T. M. O'Neil: Phys. Rev. Lett. **39** (1977) 1333.

[10] J. H. Malmberg and C. F. Driscoll: Phys. Rev. Lett. **44** (1980) 654.

[11] C. F. Driscoll and J. H. Malmberg: Phys. Rev. Lett. **50** (1983) 167.

[12] D. L. Eggleston, T. M. O'Neil and J. H. Malmberg: Phys. Rev. Lett. **53** (1984) 982.

[13] C. F. Driscoll, K. S. Fine and J. H. Malmberg: Phys. Fluids **29** (1986) 2015.

[14] D. L. Eggleston and J. H. Malmberg: Phys. Rev. Lett. **59** (1987) 1675.

[15] A. W. Hyatt, C. F. Driscoll and J. H. Malmberg: Phys. Rev. Lett. **59** (1987) 2975.

[16] C. F. Driscoll, J. H. Malmberg and K. S. Fine: Phys. Rev. Lett. **60** (1988) 1290.

[17] M. D. Tinkle, R. G. Greaves, C. M. Surko, R. L. Spencer and G. W. Mason: Phys. Rev. Lett. **72** (1994) 352.

[18] K. S. Fine, C. F. Driscoll and J. H. Malmberg: Phys. Rev. Lett. **63** (1989) 2232.

[19] C. F. Driscoll: Phys. Rev. Lett. **64** (1990) 645.

[20] Roy W. Gould and Michael A. LaPointe: Phys. Rev. Lett. **67** (1991) 3685.

[21] Roy W. Gould and Michael A. LaPointe: Phys. Fluids B **4** (1992) 2038.

[22] Roy W. Gould: Phys. Plasmas **2** (1995) 1404.

[23] Roy W. Gould: Phys. Plasmas **2** (1995) 2151.

[24] Guy Dimonte: Phys. Rev. Lett. **46** (1981) 26.

[25] R. G. Greaves, M. D. Tinkle and C. M. Surko: Phys. Rev. Lett. **74** (1995) 90.

[26] C. M. Surko, M. Leventhal and A. Passner: Phys. Rev. Lett. **62** (1989) 601.

[27] C. M. Surko and T. J. Murphy: Phys. Fluids B **2** (1990) 1372.

[28] T. J. Murphy and C. M. Surko: Phys. Rev. A **46** (1992) 5696.

[29] R. G. Greaves, M. D. Tinkle and C. M. Surko: Phys. Plasmas **1** (1994) 1439.

[30] M. D. Tinkle, R. G. Greaves and C. M. Surko: Phys. Plasmas **2** (1995) 2880.

[31] R. G. Greaves and C. M. Surko: Phys. Rev. Lett. **75** (1995) 3846.

[32] L. H. Haarsma, K. Abdullah and G. Gabrielse: Phys. Rev. Lett. **75** (1995) 806.

[33] Carl S. Weimer, J. J. Bollinger, F. L. Moore and D. J. Wineland: Phys. Rev. A **49** (1994) 3842.

[34] G. Gabrielse, X. Fei, K. Helmerson, S. L. Rolston, R. Tjoelker and T. A. Trainor: Phys. Rev. Lett. **57** (1986) 2504.

[35] K. S. Fine, C. F. Driscoll, J. H. Malmberg and T. B. Mitchell: Phys. Rev. Lett. **67** (1991) 588.

[36] T. B. Mitchell, C. F. Driscoll and K. S. Fine: Phys. Rev. Lett. **71** (1993) 1371.

[37] T. B. Mitchell and C. F. Driscoll: Phys. Rev. Lett. **73** (1994) 2196.

[38] N. Sateesh Pillai and Roy W. Gould: Phys. Rev. Lett. **73** (1994) 2849.

[39] K. S. Fine, A. C. Cass, W. G. Flynn and C. F. Driscoll: Phys. Rev. Lett. **75** (1995) 3277.

[40] C. F. Driscoll and K. S. Fine: Phys. Fluids B **2** (1990) 1359.

[41] D. H. E. Dubin and T. M. O'Neil: Phys. Rev. Lett. **60** (1988) 511.

[42] C. C. Grimes and G. Adams: Phys. Rev. Lett. **42** (1979) 795.

[43] L. R. Brewer, J.D. Prestage, J. J. Bollinger, Wayne M. Itano, D. J. Larson and D. J. Wineland: Phys. Rev. A **38** (1988) 859.

[44] D. J. Heinzen, J. J. Bollinger, F. L. Moore, Wayne M. Itano and D. J. Wineland: Phys. Rev. Lett. **66** (1991) 2080.

[45] J. J. Bollinger, D. J. Heinzen, F. L. Moore, Wayne M. Itano D. J. Wineland and Daniel H. E. Dubin: Phys. Rev. A **48** (1993) 525.

[46] J. J. Bollinger, D. J. Wineland and Daniel H. E. Dubin: Phys. Plasmas **1** (1994) 1403.

[47] F. M. Penning: Physica **3** (1936) 873.

[48] Wolfgang Paul: Rev. Mod. Phys. **62** (1990) 531.

[49] T. M. O'Neil and C. F. Driscoll: Phys. Fluids **22** (1979) 266.

[50] Daniel H. E. Dubin: Phys. Rev. Lett. **66** (1991) 2076.

[51] D. H. E. Dubin: Phys. Fluids B **5** (1993) 295.

[52] R. A. Stern and N. Tzoar: Phys. Rev. Lett. **17** (1966) 903.

[53] S. Hiroe and H. Ikegami: Phys. Rev. Lett. **19** (1967) 1414.

[54] M. Porkolab and R. P. H. Chang: Phys. Rev. Lett. **22** (1969) 826.

[55] A. Y. Wong and B. H. Quon: Phys. Rev. Lett. **34** (1975) 1499.

[56] T. M. O'Neil and J. H. Malmberg: Phys. Fluids **11** (1968) 1754.

[57] C. B. Wharton, J. H. Malmberg and T. M. O'Neil: Phys. Fluids **11** (1968) 1761.

[58] P. J. Vidmar, J. H. Malmberg and T. P. Starke: Phys. Rev. Lett. **34** (1975) 646.

[59] T. P. Starke and J. H. Malmberg: Phys. Rev. Lett. **37** (1976) 505.

[60] G. Dimonte and J. H. Malmberg: Phys. Rev. Lett. **38** (1977) 401.

[61] V. N. Tsytovich: Lectures on Non-linear Plasma Kinetics (Springer-Verlag, Heidelberg, 1995)

[62] K. Nishikawa and C. S. Liu: Asvances in Plasma Physics vol.6 (John Wiley & Sons, New York, 1967)

[63] F. F. Chen: Introduction to Plasma Physics (Plenum, New York, 1974)

[64] S. A. Prasad and T. M. O'Neil: Phys. Fluids **22** (1979) 278.

[65] A. W. Trivelpiece and R. W. Gould: J. Appl. Phys. **30** (1959) 1784.

[66] J. H. Malmberg and C. B. Wharton: Phys. Rev. Lett. **17** (1966) 175.

[67] S. A. Prasad and T. M. O'Neil: Phys. Fluids **26** (1983) 665.

[68] D. Strickland and G. Mourou: Opt. Commun. **56**, 219 (1985)

[69] W. L. Kruer: The Physics of Laser Plasma Interactions (Addison-Wesley, New York, 1988)

[70] B. C. Stuart, M. D. Feit, A. M. Rubenchik, B. W. Shore and M. D. Perry: Phys. Rev. Lett. **74**, 2248 (1995)

[71] D. von der Linde and H. Schuler: J. Opt. Soc. Am. B **13**, 216 (1996)

[72] D. Du, X. Liu, G. Kom. J.Squier and G. Mourou: Appl. Phys. Lett. **64**, 3071 (1994)

[73] B. T. V. Vu, O. L. Landen and A. Szoke: Phys. Plasmas **2**, 476 (1995)

[74] B. T. V. Vu, O. L. Landen and A. Szoke: Phys. Rev. E **47**, 2768 (1993)

[75] T. Ditmire, E. T. Gumbrell, R. A. Smith, L. Mountford M. H. R. Hutchinson: Phys. Rev. Lett. **77**, 498 (1996)

[76] R. S. Marjoribanks, F. W. Budnik, L. Zhao, G. Kulcsar, M. Stanier and J. Mihaychuk: Opt. Lett. **18**, 361 (1993)

[77] Y. B. Zel'dovich and Y. P. Raizer: Physics of Shock Waves and High-Temperature Hydrodynamic Phenomena (Academic Press, New York, 1966)

[78] X. Liu and D. Umstadter: Phys. Rev. Lett. **69**, 1935 (1992)

[79] private communication with R. Fedosejevs (Prof. University of Alberta, Canada)

[80] M. Fujita, A. A. Offenberger and C. E. Capjack: Phys. Rev. E **50**, 2175 (1994)